# STRÖMGREN SURVEY FOR ASTEROSEISMOLOGY AND GALACTIC ARCHAEOLOGY: LET THE SAGA BEGIN[*]

L. Casagrande[1,14], V. Silva Aguirre[2], D. Stello[3], D. Huber[4,5], A. M. Serenelli[6], S. Cassisi[7], A. Dotter[1],
A. P. Milone[1], S. Hodgkin[8], A. F. Marino[1], M. N. Lund[2], A. Pietrinferni[7], M. Asplund[1], S. Feltzing[9],
C. Flynn[10], F. Grundahl[2], P. E. Nissen[2], R. Schönrich[11,12,15], K. J. Schlesinger[1], and W. Wang[13]

[1] Research School of Astronomy and Astrophysics, Mount Stromlo Observatory, The Australian National University,
Canberra, ACT 2611, Australia; luca.casagrande@anu.edu.au
[2] Stellar Astrophysics Centre, Department of Physics and Astronomy, Aarhus University, Ny Munkegade 120, DK-8000 Aarhus C, Denmark
[3] Sydney Institute for Astronomy (SIfA), School of Physics, University of Sydney, Sydney, NSW 2006, Australia
[4] NASA Ames Research Center, Moffett Field, CA 94035, USA
[5] SETI Institute, 189 Bernardo Avenue, Mountain View, CA 94043, USA
[6] Institute of Space Sciences (IEEC-CSIC), Campus UAB, Fac. Ciéncies, Torre C5 parell 2, E-08193 Bellaterra, Spain
[7] INAF-Osservatorio Astronomico di Collurania, via Maggini, I-64100 Teramo, Italy
[8] Institute of Astronomy, Madingley Road, Cambridge CB3 0HA, UK
[9] Lund Observatory, Department of Astronomy and Theoretical Physics, P.O. Box 43, SE-22100 Lund, Sweden
[10] Centre for Astrophysics and Supercomputing, Swinburne University of Technology, Hawthorn, VIC 3122, Australia
[11] Department of Astronomy, The Ohio State University, 140 West 18th Avenue, Columbus, OH 43210-1173, USA
[12] Rudolf-Peierls Centre for Theoretical Physics, University of Oxford, 1 Keble Road, Oxford OX1 3NP, UK
[13] National Astronomical Observatories, Chinese Academy of Sciences, Beijing 100012, China

## ABSTRACT

Asteroseismology has the capability of precisely determining stellar properties that would otherwise be inaccessible, such as radii, masses, and thus ages of stars. When coupling this information with classical determinations of stellar parameters, such as metallicities, effective temperatures, and angular diameters, powerful new diagnostics for Galactic studies can be obtained. The ongoing Strömgren survey for Asteroseismology and Galactic Archaeology has the goal of transforming the *Kepler* field into a new benchmark for Galactic studies, similar to the solar neighborhood. Here we present the first results from a stripe centered at a Galactic longitude of 74° and covering latitude from about 8° to 20°, which includes almost 1000 K giants with seismic information and the benchmark open cluster NGC 6819. We describe the coupling of classical and seismic parameters, the accuracy as well as the caveats of the derived effective temperatures, metallicities, distances, surface gravities, masses, and radii. Confidence in the achieved precision is corroborated by the detection of the first and secondary clumps in a population of field stars with a ratio of 2 to 1 and by the negligible scatter in the seismic distances among NGC 6819 member stars. An assessment of the reliability of stellar parameters in the Kepler Input Catalog is also performed, and the impact of our results for population studies in the Milky Way is discussed, along with the importance of an all-sky Strömgren survey.

*Key words:* Galaxy: stellar content – stars: abundances – stars: distances – stars: fundamental parameters – stars: oscillations – surveys – techniques: photometric

*Online-only material:* color figures, machine-readable table

## 1. INTRODUCTION

The study of a sizeable number of individual stars in the Milky Way enables us to directly access different phases of its formation and evolution in a fashion that is still hardly achievable for external galaxies. For obvious reasons, stars in the vicinity of the Sun have been preferred targets for this purpose, from the very first (e.g., Gliese 1957; Wallerstein 1962; van den Bergh 1962; Eggen et al. 1962) to the most recent photometric and spectroscopic investigations of the Milky Way, for which *Hipparcos* astrometric distances are also available out to ≃100 pc (e.g., Nordström et al. 2004; Reddy et al. 2006; Feltzing & Bensby 2008; Casagrande et al. 2011; Adibekyan et al. 2013; Bensby et al. 2014). Properties of stars in the solar neighborhood, in particular ages and metallicities, are still the

main constraint for Galactic chemo(dynamical) models (e.g., Cescutti et al. 2007; Schönrich & Binney 2009; Kobayashi & Nakasato 2011; Minchev et al. 2013; Wang & Zhao 2013) and provide important clues to understanding the main processes at play in galaxy formation and evolution (e.g., Pilkington et al. 2012; Bird et al. 2013).

This sort of study is now fostered by a number of spectroscopic and photometric surveys, targeting different and fainter components of the Milky Way (e.g., RAdial Velocity Experiment (RAVE): Steinmetz et al. 2006; Sloan Digital Sky Survey (SDSS)–Sloan Extension for Galactic Understanding and Exploration (SEGUE): Yanny et al. 2009; SDSS–APOGEE: Ahn et al. 2014; Vista Variables in the Via Lactea (VVV): Minniti et al. 2010; *Gaia-ESO:*Gilmore et al. 2012; GALactic Archaeology with HERMES (GALAH): Freeman & HERMES/GALAH Team 2014), although astrometric distances for the targets in these surveys will not be available until the *Gaia* spacecraft releases its data (Lindegren & Perryman 1996; Perryman et al. 2001). A common feature of all past and current stellar surveys is that while it is relatively straightforward to derive some sort of

---

information on the chemical composition of the targets observed (and in many cases even detailed abundances), that is not the case when it comes to masses, radii, distances, and, in particular, ages. Even when accurate astrometric distances are available to allow comparison of stars with isochrones, the derived ages are still highly uncertain, and statistical techniques are required to avoid biases (e.g., Pont & Eyer 2004; Jørgensen & Lindegren 2005). Furthermore, isochrone dating is meaningful only for stars in the turnoff and subgiant phase, where stars of different ages are clearly separated on the H-R diagram. This is in contrast, for example, to stars on the red giant branch (RGB), where isochrones with vastly different ages can fit equally well observational constraints such as effective temperatures, metallicities, and surface gravities within their errors (see, e.g., Soderblom 2010 for a review). Thus, alternative ways to precisely determine masses and radii of stars are the only way forward.

By measuring oscillation frequencies in stars, asteroseismology allows us to determine fundamental physical quantities, in particular masses and radii, that otherwise would be inaccessible in single field stars and that can be used to obtain information on stellar distances and ages (see, e.g., Chaplin & Miglio 2013 for a review). Individual frequencies can yield an accuracy of just a few percent on those parameters, but their exploitation is more demanding, both observationally and theoretically (Silva Aguirre et al. 2013). Global asteroseismic observables (see Section 3.5), on the contrary, are easier to detect and analyze yet are able to provide the aforementioned parameters for a large number of stars with an accuracy that is still much better than achievable by isochrone fitting in the traditional sense. Thanks to spaceborne missions such as *CoRoT* (Baglin & Fridlund 2006) and *Kepler* (Gilliland et al. 2010), average oscillation frequencies are now robustly detected in more than 500 main-sequence and subgiant stars and over 13,000 giants (e.g., De Ridder et al. 2009; Verner et al. 2011; Stello et al. 2013). Asteroseismology is thus emerging as a new tool for studying stellar populations, and initial investigations in this direction have already been done (Chaplin et al. 2011; Miglio et al. 2013a). However, until now asteroseismic studies of stellar populations had only coarse information on "classical" stellar parameters such as $T_{\rm eff}$ and [Fe/H]. Coupling classical parameters with seismic information not only improves the seismic masses and ages obtained for stars (Lebreton & Montalbán 2009; Chaplin et al. 2014) but also allows us to address important questions in stellar and Galactic evolution.

To fully harvest the potential that asteroseismology brings to these studies, classical stellar parameters are vital yet unavailable for a large sample of stars with detected oscillations. The main purpose of the Kepler Input Catalog (KIC; Brown et al. 2011) was to separate dwarfs from giants, and it is therefore inadequate for high-precision stellar and Galactic studies because of significant biases in its stellar parameters (e.g., Molenda-Żakowicz et al. 2011; Pinsonneault et al. 2012; Thygesen et al. 2012). The APO Galactic Evolution Experiment (APOGEE) will eventually provide parameters for thousands of *Kepler* giants, and, similarly, the *Gaia*-ESO Survey and GALAH will provide them for the *CoRoT* fields. The advantages of the spectroscopic surveys are obvious, yet photometry still offers a powerful and complementary alternative.

Here we present the first results from the ongoing Strömgren survey for Asteroseismology and Galactic Archaeology (SAGA) in the *Kepler* field. The goals of our photometric survey are manifold. First, the Strömgren system was envisaged with the ultimate purpose of studying Galactic stellar populations and was designed to provide reliable stellar parameters, in particular metallicities (Strömgren 1963, 1987). Thus, even compared to multifiber spectroscopy, wide-field Strömgren imaging is very efficient. It also has the advantage that no preselection is made on targets: all stars that fall in a given brightness regime across the instrument field of view will be observed. This greatly simplifies the selection function, which in our case is essentially dictated by the *Kepler* satellite (e.g., Batalha et al. 2010; Farmer et al. 2013). Further, relatively faint magnitudes can be probed at high precision even on a small-class telescope, making it possible to readily derive metallicities over a large magnitude range. The *Kepler* seismic sample presented in this work can thus be used as reference, e.g., for assessing the accuracy at which stellar parameters can be obtained for stars having only photometric measurements, such as the planet host stars we observe in SAGA. At the same time, the sensitivity of Strömgren colors to metallicity, coupled with seismic ages, helps immensely in calibrating other metallicity and age-dating techniques, thus creating powerful new tools to study more remote Galactic populations than previously possible. Bearing in mind the expected precision at which *Gaia* will deliver astrophysical parameters for stars of different brightness (Liu et al. 2012), the above science case highlights the importance of having an all-sky Strömgren survey going fainter than any of the current large spectroscopic surveys (Wang et al. 2014).

The SAGA survey also represents a natural extension of the Geneva–Copenhagen Survey (GCS; Nordström et al. 2004), the only all-sky Strömgren survey currently available, and a benchmark for Galactic studies. Similar to our latest revision of the GCS (Casagrande et al. 2011), we combine Strömgren metallicities with broadband photometry to obtain effective temperatures ($T_{\rm eff}$) and metallicities ([Fe/H]) for all our targets via the infrared flux method (IRFM). This facilitates the task of placing SAGA and GCS on the same scale. However, there are marked differences between the two surveys: the GCS is an all-sky, shallow survey limited to main-sequence and subgiant stars closer than $\simeq$100 pc (40 pc volume limited). The *Kepler* targets observed by SAGA are primarily giants located between $\simeq$1 and $\simeq$6 kpc in a specific region of the Galactic disk (Figures 1 and 2). The use of giants as probes of Galactic archaeology is possible since it is relatively straightforward to derive ages for these stars once classical stellar parameters are coupled with asteroseismology. This was not the case for the GCS, where isochrone fitting was used, and thus, GCS was limited to main-sequence and subgiant stars with known astrometric distances. On the other hand, stars in the GCS have kinematic information, which is not available for the SAGA targets. The different distance ranges sampled by the GCS and SAGA make them complementary: the stellar properties measured within the solar neighborhood in the former survey can be dynamically stretched across several kiloparsecs using kinematics. In contrast, the larger distance range sampled by the giants in SAGA provides in situ measurements of various stellar properties over $\simeq$5 kpc.

In this paper we present the observing strategy and data reduction of the Strömgren survey. After cross-matching this data set with stars in the *Kepler* field with seismic information, we derive classical and seismic stellar parameters for almost 1000 targets. Our approach is characterized by the powerful combination of classical and seismic parameters, to our knowledge the first of this kind, and a careful treatment of the errors, allowing us to derive self-consistent effective temperatures, distances, masses, and radii with a typical precision of a few percent, in addition to metallicities as we discuss in more detail later. With these
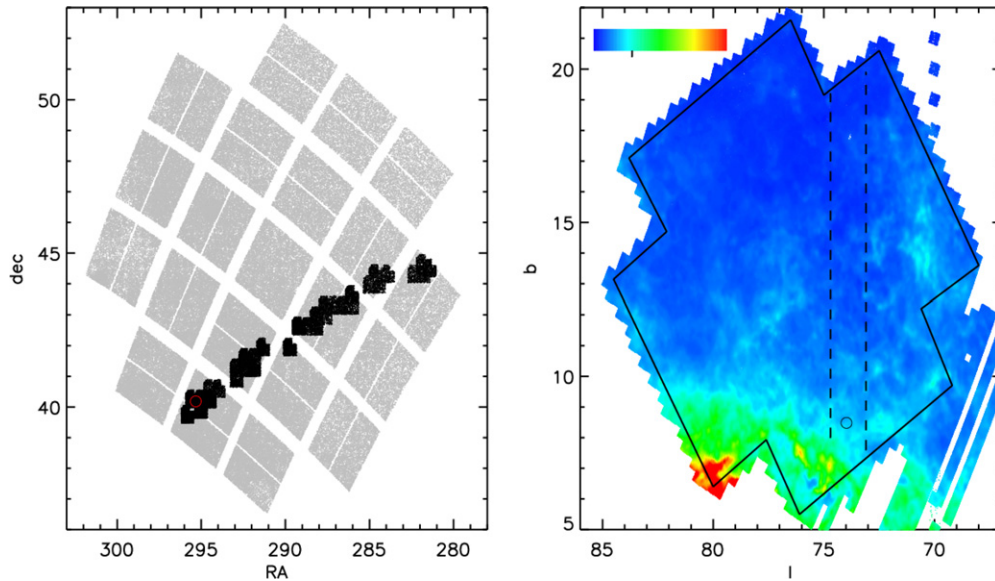
**Figure 1.** Left: the *Kepler* field as seen via the 42 CCDs on board the spacecraft. Overplotted in black is the full sample of stars with *uvby* magnitudes measured during the first run of the SAGA survey. The circle marks the position of the open cluster NGC 6819. Right: *Kepler* field (defined with continuous black lines) plotted in Galactic latitude ($b$) and longitude ($l$) as seen in the Schlegel et al. (1998) map. The linear color code corresponds to reddening in the range $0 < E(B - V) < 1$. The tick mark in the upper bar identifies $E(B - V) = 0.3$, which is the highest value in the Schlegel et al. (1998) map over our observed stripe. Vertical dashed lines mark the observed stripe, and the open circle indicates the position of NGC 6819.

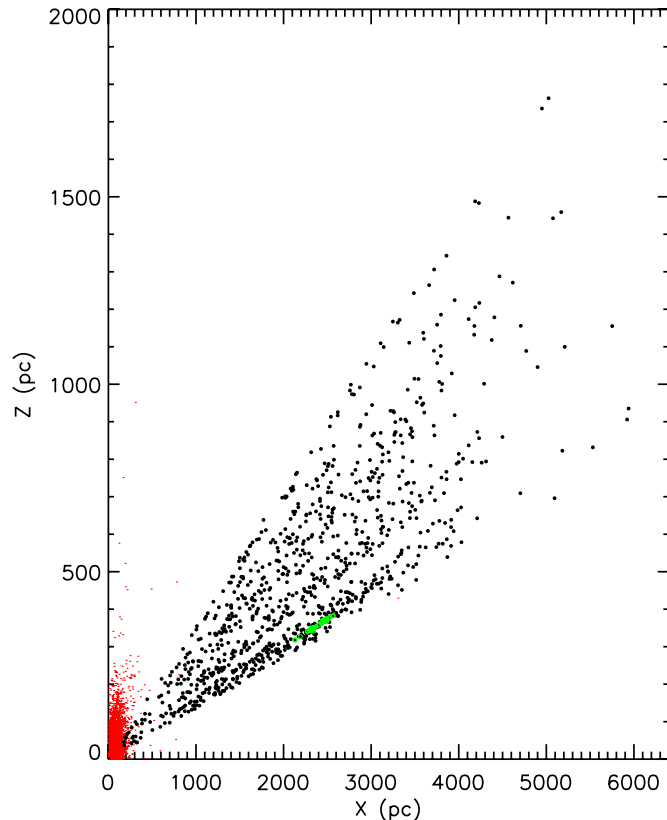(A color version of this figure is available in the online journal.)



**Figure 2.** Distance distribution for all seismic targets currently in SAGA. Overplotted in red is the volume surveyed by the Geneva–Copenhagen Survey. Highlighted with green open circles are giants belonging to NGC 6819. Distances have been derived as described in Section 3.

(A color version of this figure is available in the online journal.)

parameters in hand, stellar ages are a straightforward by-product, although more caution must be used: we leave their estimation to a subsequent publication.

## 2. THE STRÖMGREN SURVEY

The *uvby* photometric system (Strömgren 1963) is designed for the determination of basic stellar atmospheric parameters through the color indices $(b - y)$, $m_1 = (v - b) - (b - y)$, and $c_1 = (u - v) - (v - b)$. The $y$ magnitude is defined to be essentially the same as Johnson *V* for stars other than M type, and the color $(b - y)$ is relatively unaffected by line blanketing and thus is well suited for measuring effective temperatures (although in this study we will determine $T_{\rm eff}$ in a more fundamental way by using broadband photometry in the IRFM; see Section 3.1). The $m_1$ index is designed to measure the depression due to metal lines around 4100 Å ($v$ band) and hence is suitable to infer the metallicity of a variety of stars. Finally, the $c_1$ index is designed to evaluate the Balmer discontinuity, which is a temperature indicator for B- and A-type stars and a surface gravity indicator for late-type stars, although for stars with temperature lower than or comparable to the Sun it also carries metallicity information (see, e.g., Bessell 2005; Önehag et al. 2009; Árnadóttir et al. 2010 and references therein).

### 2.1. Observations and Data Reduction

Intermediate-band Strömgren *uvby* photometry was obtained during seven nights with the Wide Field Camera on the 2.5 m Isaac Newton Telescope on La Palma. The camera comprises four 2k × 4k thinned EEV CCDs; the coverage of each of the chips is 22.8 × 11.4 arcmin for a total field of view of 34 × 34 arcmin. Pixel size is 13.5 $\mu$m, corresponding to 0.33 arcsec pixel$^{-1}$, thus making the instrument ideal for wide-field optical imaging surveys (e.g., Drew et al. 2005; Groot et al. 2009; Greiss et al. 2012).

Of the seven nights awarded during period 2012A, only four provided useful data because of bad weather on the other nights. Typical seeing during the four good nights was about 1.1 arcsec, implying a typical FWHM of the stellar point-spread function (PSF) of 3–4 pixels.

Strömgren standard stars were chosen from the list of Schuster & Nissen (1988), which is carefully tied to the system used by Olsen (1983) and underlying the GCS used for our previous investigation of stellar properties in the Galactic disk (Casagrande et al. 2011). We use secondary rather than primary Strömgren standards as the latter are too bright to observe with a 2.5 m telescope. Throughout each of the four photometric nights 10 standard stars were usually observed multiple times over a large span of magnitude and color indices and at different elevations in the sky, bracketing pointings on the *Kepler* field both in air mass and time.

A stripe across the *Kepler* field was observed, covering Galactic latitude $7\overset{\circ}{.}6 < b < 19\overset{\circ}{.}9$ and centered at Galactic longitude $l = 74°$. About 60% of the pointings were observed more than once on at least two different photometric nights. We chose a tiling strategy with an overlap of $\simeq 3$ to $\simeq 10$ arcsec between different pointings over the *Kepler* field, thus allowing us to check that photometric zero points are constant over the observed region. This strategy allows us to uniformly sample the Galactic disk, as encompassed by the field of view of *Kepler*. The lower limit on $b$ is set to avoid regions too close to the plane, where crowding and reddening make it more difficult to use photometric data. The choice of the Galactic longitude upon which our stripe is centered was dictated by the fact that while this region is only moderately affected by dust and obscuration, it also includes the open cluster NGC 6819, which provides a useful benchmark, as discussed later.

The purpose of the SAGA survey is to obtain accurate Strömgren photometry for stars in the magnitude range $10 \lesssim y \lesssim 14$, where *Kepler* is able to detect oscillations in most red giant stars (e.g., Huber et al. 2011). For science pointings, a typical observing sequence comprised one short ($\simeq$5–10 s) and one long (30–60 s) exposure in $vby$ and two short ($\simeq$30 s) and one long ($\simeq$120 s) in $u$, after which a 45 arcsec dither was applied and the above cycle was repeated. With this strategy we are able to achieve photometric errors <0.03 mag in all bands over the magnitude range of interest (see Figure 4 below), which is the accuracy needed to obtain robust parameters from Strömgren indices (e.g., Calamida et al. 2007). However, useful stellar properties can still be derived down to 16th magnitude, a regime important for planet-candidate host stars (Batalha et al. 2013; Plavchan et al. 2014).

The images of the *Kepler* field and the standard stars were preprocessed with the Wide Field Survey Pipeline provided by the Cambridge Astronomical Survey Unit (Irwin & Lewis 2001). The operations applied to the images were debiasing, trimming, flat fielding, and correction for nonlinearity.

### 2.2. Standard Stars: Photometric Calibration

Aperture photometry for standard stars was obtained with the task PHOT within the IRAF[16] DAOPHOT package. For each star we explored different sizes of the aperture, ranging from 5 to 20 pixels, and found a value of 15 to be optimal. This roughly corresponds to 4–5 × FWHM of the typical stellar PSF, and it is ideal for well-isolated standards as in our case (e.g., Massey & Davis 1992). In order to transform instrumental (inst) into standard magnitudes, we adopted the following equation for each of the Strömgren filters ($i = u, v, b, y$).

$$m_{\text{inst},i} = m_i + \epsilon_{1,i}X + \epsilon_{2,i}(m_v - m_y) + \epsilon_{3,i}T + \epsilon_{4,i}, \quad (1)$$

where $X$ and $T$ denote the air mass and time of that CCD exposure and $m_v - m_y$ is the color of the standard system (e.g., Harris et al. 1981; Grundahl et al. 2002). The terms $\epsilon_{1,i}, \ldots, \epsilon_{4,i}$ were determined individually for each photometric night; cross-checks for stars in common observed over different nights confirm these terms are stable to better than 0.01 mag in each band. We found the $\epsilon_{3,i}$ time term to be significant in $u$ and $v$, although essentially negligible in $b$ and $y$. For the sake of our discussion, Equation (1) can be rewritten highlighting only the color term,

$$m_{\text{inst},i} = m_i + \epsilon_{2,i}(m_v - m_y) + k_i, \quad (2)$$

where $k_i$ now includes all previous air mass, time, and zero-point terms.

As customary with CCD photometry, the transformation to the standard system is done using individual magnitudes rather than Strömgren indices since each filter is observed separately and hence with a time delay. This is in contrast to four-channel photometry where observations for all four filters are obtained at the same time, also allowing observations during nonphotometric nights (e.g., Olsen 1983; Schuster & Nissen 1988; Meléndez et al. 2010). Calibrating upon individual magnitudes has the advantage that we need not worry that observations through the different filters are obtained at different air masses for each standard star. Figure 3 shows the residual between our photometry and the standard stars: excellent agreement is obtained in all four filters with small scatter and no obvious trends as a function of $(v - y)$. The same check using other color combinations also shows no trends.

### 2.3. Science Stars: Photometric Calibration

Aperture photometry was done on each of the science images separately. A dedicated suite of scripts has been developed for this purpose, as described below. Coordinate lists for the images in each band were created using the IRAF task DAOFIND. Aperture photometry was done with apertures ranging from 5 to 20 pixels in steps of 1 pixel. Flux and photometric errors (the `merr` output in PHOT, essentially determined from photon statistics) of each source were extracted at all selected apertures. For each image we searched for the brightest stars above a predefined instrumental magnitude, having `merr` <0.015 mag and separated from any other detected source by at least twice the maximum aperture.[17] An iterative scheme was employed to move the brightness threshold to fainter magnitudes if less than 10 such stars were identified. These stars were then used to compute the curve of growth, which was found to remain essentially constant for apertures larger than 15 pixels. The aperture correction was then computed for each frame as the median of the flux ratio measured in an aperture of 15 and 5 pixels, using a 2.6$\sigma$ clipping to remove outliers. The mean absolute deviation was used to define $\sigma$, which together with the median described above provides robust statistics on our definition of the aperture correction. In this way, we also determined for each magnitude the systematic error stemming from the uncertainty $\sigma$ in the aperture correction. This procedure was run in an iterative mode by checking in each frame the position of bright stars on the CCDs and the resulting curve of growth. In all instances, results were found to be robust, with no need for further human intervention, thus making it possible to run the entire procedure in batch mode. For each frame,

---

[17] More precisely, by twice the annulus plus dannulus as defined in DAOPHOT.
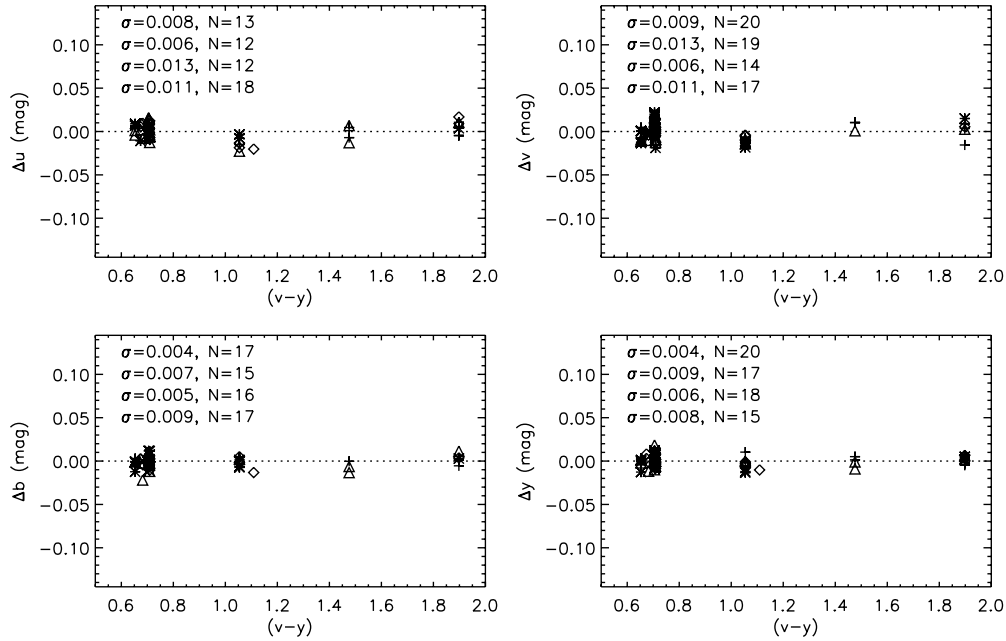
**Figure 3.** Residuals of the standard stars (calibrated minus standard) as a function of their $(v - y)$ color. The number of points ($N$) and the scatter ($\sigma$) for each photometric night (different symbol for each night) are indicated.

astrometric solutions were computed using the World Coordinate System from the image header and correcting for field distortion. By cross-matching the position of several of the brightest targets against the Two Micron All Sky Survey (2MASS), we conclude the astrometric precision for our coordinates is 0.2–0.3 arcsec.[18] In very few cases (less than 1%) the astrometric solutions were found to differ from 2MASS coordinates with trends depending on the X and Y positions on the CCD; those images were excluded from further analysis. For each object identified in each frame, the right ascension (R.A.) and declination (decl.) distance with respect to all other objects identified in subsequent frames and filters was computed: the vast majority of distances cluster into an ellipse of axis 0.4 arcsec in R.A. and 0.3 arcsec in decl., which is thus the typical accuracy at which a given object is identified in different frames and filters. This search ellipse was used to match sources in different bands and frames throughout the remainder of the data reduction.

By matching sources in different filters, we are thus able to apply the photometric calibration to the standard system. Notice, however, that Equation (2) depends on the standard color $m_v - m_y$, which for science targets is not known beforehand. Therefore, we first solved for $m_v$ and $m_y$,

$$\begin{pmatrix} m_v \\ m_y \end{pmatrix} = \begin{pmatrix} 1 + \epsilon_{2,v} & -\epsilon_{2,v} \\ \epsilon_{2,y} & 1 - \epsilon_{2,y} \end{pmatrix}^{-1} \begin{pmatrix} m_{\text{inst},v} - k_v \\ m_{\text{inst},y} - k_y \end{pmatrix}, \quad (3)$$

such that Equation (2) could be applied to $m_u$ and $m_b$ afterward. For each night, calibrated photometry for each frame in a given filter was cross-matched for stars in common with all other frames in the same filter. We then calculated the median offset with respect to all other images for each frame; zero-point differences were, on average, a few millimagnitudes (thus confirming the stability of our measurements on photometric nights), apart from occasional offsets spurring to several hundredths (or more) of a magnitude. The median is essentially unaffected by the presence of strong outliers, and an iterative scheme was employed to bring all frames to exactly the same

zero point, whichever of the following conditions was first satisfied: an average median offset with respect to all other frames in the same filter and in the same night reached below 0.005 mag or we reached at least seven iterations. This second condition was chosen to avoid the rare cases when the zero-point correction oscillates just above the 0.005 mag threshold since convergence within 0.01 mag is always reached within three or four iterations at most. This zero-point shift for each frame was included as a systematic uncertainty in all the photometric values of that given frame. Since Equations (2) and (3) depend on the standard $m_v - m_y$ color, those were reapplied after correcting for the zero points determined above.

The photometric error associated with each measurement was derived from the sum of squared residuals stemming from photon statistics, aperture correction uncertainty, and the zero-point shifts described above. If more than one measurement was available, then the weighted average (using the above photometric error as weight) was used, and the standard deviation was taken as measurement error. On the basis of these global photometric errors, we define fiducials for selecting stars with the most reliable photometry; those ridgelines are shown in Figure 4. A star is flagged to have good photometry only if the errors in all four bands fall below those ridgelines.

Since we are interested in determining $uvby$ for all stars, we took $u$-band measurements (our faintest band) and searched for matches in all other filters. The coordinate of each object having Strömgren magnitudes was determined by computing the average coordinate from $uvby$ bands, using the standard deviation as the uncertainty. The final catalog contains 29,521 sources with $uvby$ measurements (all shown in Figure 4). Changing the matching criterion to a circular search of radius 1 arcsec returns essentially the same number of objects (29,496).

### 2.4. Comparison with Other Strömgren Studies

The only all-sky Strömgren survey is the GCS, which is largely based on the extensive work of Olsen (1983, 1984, 1994a, 1994b) upon which we ought to calibrate. Most of the stars in the GCS are brighter than our saturation limit and are
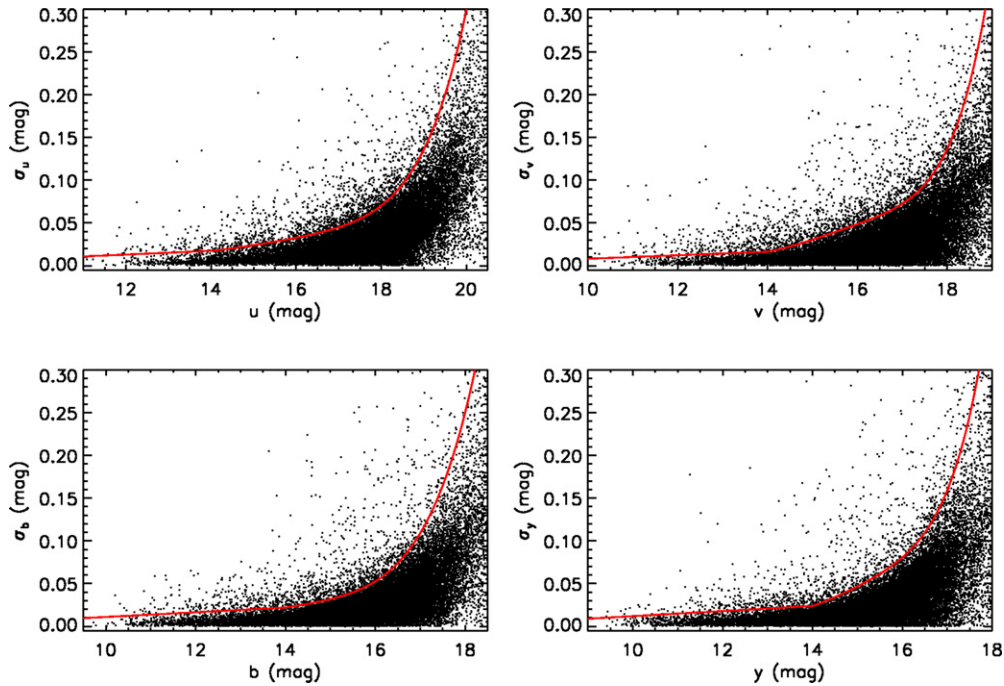
---

**Figure 4.** Final errors in $u$, $v$, $b$, and $y$ photometry. Stars above the continuous ridgelines are labeled in the analysis as explained in Section 2.3.

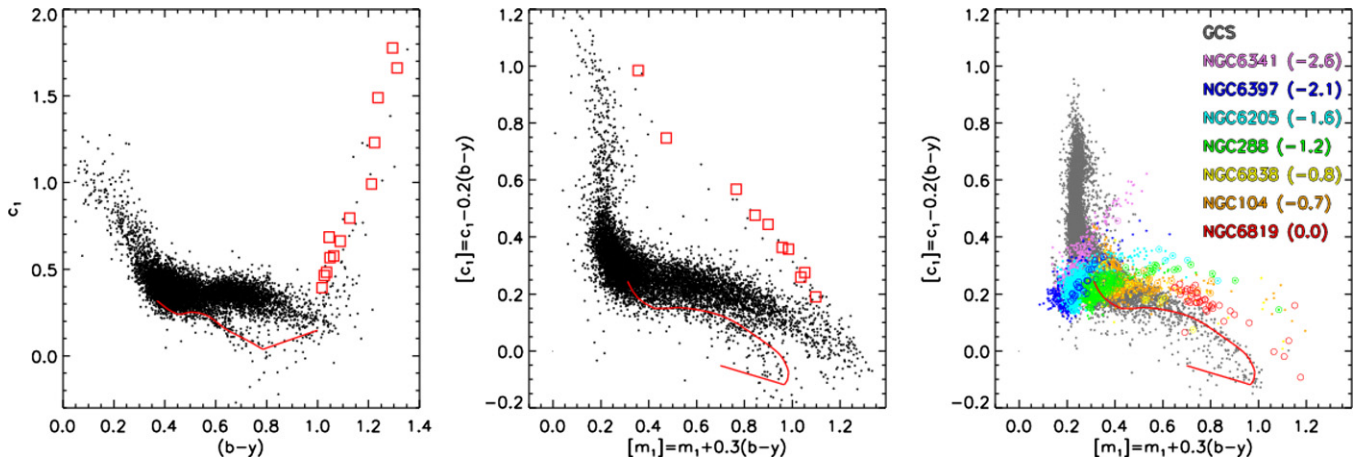(A color version of this figure is available in the online journal.)



**Figure 5.** Left: $c_1$ vs. $(b - y)$ diagram for stars in our sample with $y < 15$ mag and photometric errors below the ridgelines of Figure 4. Open squares are cool M giants, while the continuous line represents the dwarf sequence, both from Olsen (1984). Middle: same as in the left panel, but for reddening-free indices $[c_1]$ vs. $[m_1]$. Right: reddening-free indices for dwarfs and subgiants from the GCS as well as for a number of RGB stars in stellar clusters (metallicities in parentheses), all standardized to the system of Olsen. Open circles are stars with spectroscopic [Fe/H] used for our giant metallicity calibration.

(A color version of this figure is available in the online journal.)

sparsely distributed across the entire sky, resulting in no object in common with our observations. However, we can easily verify if our observations follow the mean loci of good Strömgren photometry in the Olsen system. In the left panel of Figure 5, we plot our measurements in the $c_1$ versus $(b - y)$ plane, which discriminates between dwarfs and giants (e.g., Faria et al. 2007; Adén et al. 2009). Overplotted is the fiducial dwarf sequence from Olsen (1984), which is well matched by our stars.[19] Because of the relatively bright magnitude range we sample, most of the late-type stars are actually giants (see the left panels

in Figure 9, where most of the stars in the bright magnitude range encompassed by dotted lines are, in fact, giants). Our sample is spread across several degrees in the Galactic latitude, where reddening varies from a few hundredths to over a tenth of a magnitude (see Section 3.3). In the middle panel, we thus use the virtually reddening-free indices $[c_1] = c_1 - 0.2(b - y)$ and $[m_1] = m_1 + 0.3(b - y)$ (e.g., Strömgren 1966; Crawford 1975; Olsen 1984). It is clear that cool dwarfs are separated from giants and that there are a few cool M giants in our sample. For reference, in the right panel, we also plot all dwarfs and subgiants from the GCS (which were observed by Olsen), a number of RGB stars from globular clusters of different metallicities (Grundahl et al. 1998, 2000, 2002; all standardized to the Olsen system), and our own observations of the open cluster NGC 6819 in the *Kepler* field. Again, dwarf stars follow

---

[19] Fiducials for different metallicities have recently been obtained by Árnadóttir et al. (2010); here, we use that of Olsen (1984) for the sake of comparing directly with the original system.

Olsen's fiducial, while giants define upper sequences according to their metallicities.

## 3. DETERMINATION OF STELLAR PARAMETERS FOR *KEPLER* TARGETS

The purpose of the SAGA survey is to uniformly observe all stars across the *Kepler* field down to $V$ of 15th to 16th magnitude, independent of whether or not they have seismic information. We cross-match all stars with measured Strömgren photometry from the previous section with all seismic targets in the *Kepler* field of view, i.e., $\simeq 15{,}000$ giants from the *Kepler* Asteroseismic Science Consortium (Stello et al. 2013; Huber et al. 2014) and over 500 dwarfs (Chaplin et al. 2014). We detect about 95% of the seismic targets falling in the region sampled by SAGA so far, totaling 1010 targets (29 dwarfs and 981 giants). Further cross-matching of the sample with optical and infrared broadband photometry (for the sake of the IRFM; see Section 3.1) and seismic analysis reduce the sample for which we determine full parameters to 989 stars, implying a completeness of 93% for our final catalog. Most of the stars in our sample are giants (see also Figure 17), but the procedure we adopt for determining parameters is the same whether a star is a dwarf or a giant (apart from the metallicity calibration; see Section 3.2).

Multiband photometry of stars in the *Kepler* field allows us to choose the most appropriate set of filters for each of the stellar parameters we wish to determine. One of the key advantages of our approach is that we use seismic information to improve upon the determination of photometric quantities. All parameters described in the following are derived iteratively and in a fully self-consistent manner, following the procedure first presented in Silva Aguirre et al. (2011, 2012) and briefly summarized here. Details on each step are described in the relevant subsections.

Broadband optical and infrared photometry is used to obtain effective temperatures ($T_{\rm eff}$), bolometric fluxes ($\mathcal{F}_{\rm Bol}$), and angular diameters ($\theta$) of each star via the IRFM (Section 3.1). This method depends weakly on the metallicity and surface gravity of a star, rendering it ideal for breaking the degeneracy among these parameters, which instead seriously affects spectroscopic methods (e.g., Alonso et al. 1996; Casagrande et al. 2006). However, being a photometric technique, reddening must be properly taken into account. For each star in our sample, we first take the color excess $E(B-V)$ and $\log g$ from the KIC (Brown et al. 2011), while keeping metallicity fixed at [Fe/H] $= -0.2$, a value assumed to be roughly representative of the *Kepler* field (e.g., Silva Aguirre et al. 2011; Pinsonneault et al. 2012; Chaplin et al. 2014). These parameters are used as a starting point, but all our solutions converge independently of the initial choice. The effective temperature is derived using the IRFM with these initial $\log g$, [Fe/H], and $E(B-V)$. This $T_{\rm eff}$ is then fed into an asteroseismic Bayesian scheme to obtain the mass and the radius of each star (Section 3.5). Scaling $\theta$ with the asteroseismic radius, we compute the distance (Silva Aguirre et al. 2012). Using empirically calibrated, three-dimensional Galactic extinction models (Section 3.3), this distance is used to derive a new $E(B-V)$, which is then used to deredden the *uvby* photometry and derive Strömgren metallicities (Section 3.2). The above series of steps defines one iteration, the updated set of $E(B-V)$, $\log g$, and [Fe/H] determined at its completion is fed into the IRFM anew, and the procedure outlined above is repeated until convergence is reached in all parameters: this was achieved within three iterations.

We note that in addition to our Strömgren photometry (used exclusively for deriving [Fe/H]), three broadband systems are used in the IRFM: this implies three slightly different sets of $T_{\rm eff}$, $\mathcal{F}_{\rm Bol}$, and $\theta$. Therefore, three sets of seismic parameters, distances, and thus reddening estimates (and [Fe/H]) are obtained even if the same reddening map is used. Within a given map, all these differences are relatively small.

Altogether we explore the use of three different broadband photometric systems and three reddening maps for a total of nine different self-consistent combinations of parameters. The effect of adopting different stellar models and pipelines for the seismic analysis has also been investigated. By comparing these values, we are able to obtain realistic error bars (Section 3.7) as well as robust final parameters (Section 3.8). A flowchart illustrating the entire procedure is shown in Figure 6; in the following subsections we describe each step in detail, focusing first on the derivation of classical parameters and turning then to the asteroseismic analysis.

We next discuss the rationale behind our choice of using different approaches to determine different stellar parameters, instead of, for example, implementing a global minimization scheme to match all photometric and seismic observables simultaneously. As described in the relevant subsections, effective temperatures, angular diameters, metallicities, and reddening are determined using well-established and almost entirely empirical techniques. These empirically determined quantities are then fed into a Bayesian scheme built upon a grid of theoretical models. Extending this Bayesian scheme to include observed photometric indices would make the determination of classical stellar parameters entirely dependent on theoretical models. In addition, it would carry uncertainties related to the standardization of synthetic colors (which are usually small) as well as to model flux deficiencies and/or uncertainties. The latter can be nonnegligible in intermediate-band filters, as well as toward the blue and ultraviolet wavelengths (Casagrande & Vanden-Berg 2014). In our case, the dependence on synthetic flux is minimized by the multiple-broadband photometry, as well as by the use of fully empirical calibrations in the intermediate-band Strömgren system.

### 3.1. Effective Temperatures and Angular Diameters

Effective temperatures are derived using the IRFM described in Casagrande et al. (2010). This technique uses multiband optical and infrared photometry to recover the bolometric and infrared flux of each star, from which its $T_{\rm eff}$ and $\theta$ can be computed. In our original formulation, implementing either *Tycho*2–2MASS or Johnson-(Cousins)–2MASS photometry, the zero point of the effective temperature scale is secured via solar twins, and the reliability of the angular diameters is checked against dwarf and subgiant stars with interferometric measurements. This technique has already been used in a number of *Kepler* investigations (e.g., Silva Aguirre et al. 2011, 2012; Huber et al. 2012; Chaplin et al. 2014), and its accuracy is now extended and validated also for giants (Casagrande et al. 2014).

Here we implement the IRFM with three different optical systems (KIC $griz$, Johnson $BV$, and Sloan $g'r'i'$), while in all instances 2MASS photometry is used in the infrared. While we defer more details on the quality of 2MASS photometry to Section 3.6, here it suffices to recall its excellent accuracy, with both median and mean errors of only 0.02 mag in all three infrared bands. The implementation of the IRFM in the KIC $griz$–2MASS system is anchored to *Tycho*2–2MASS, requiring
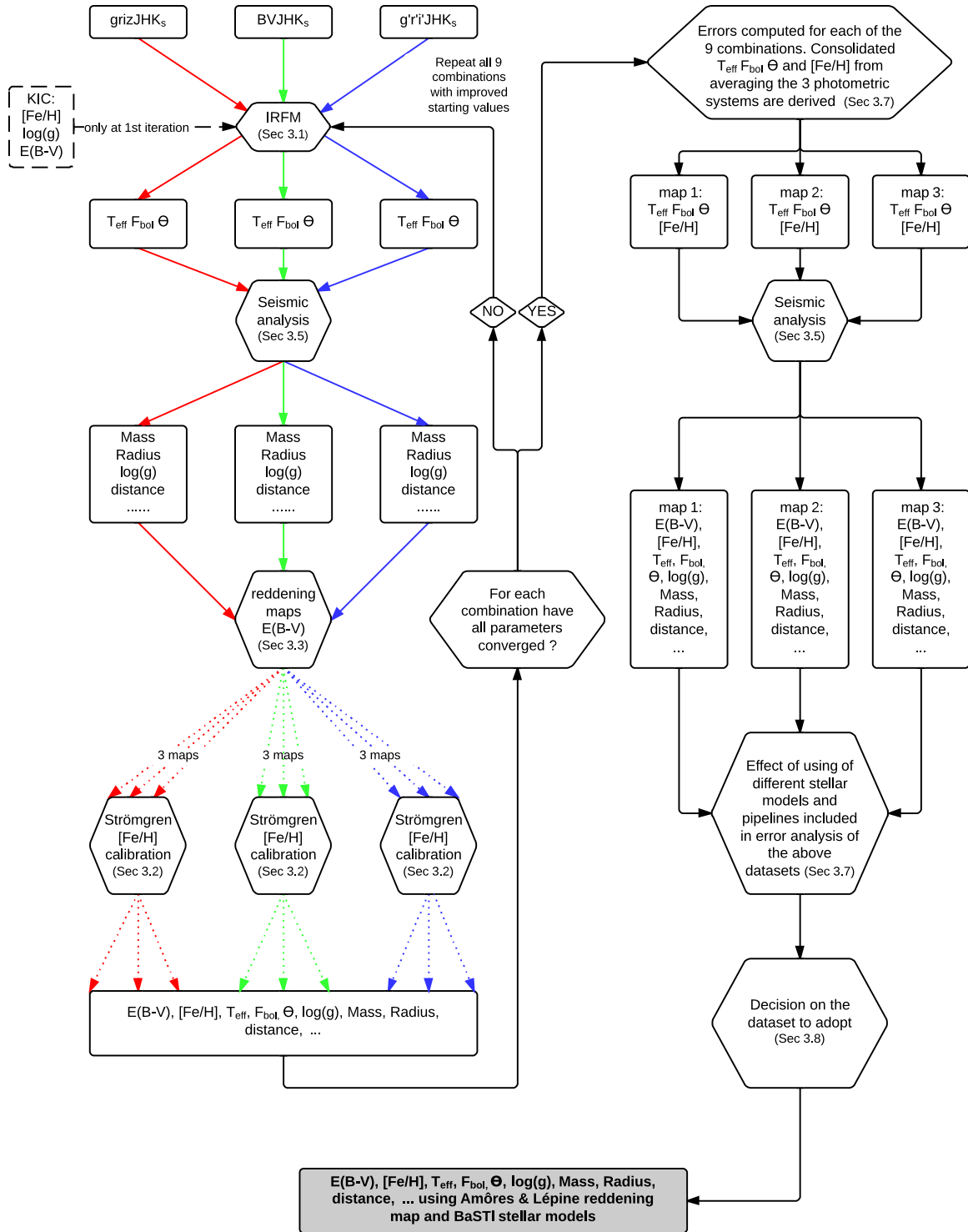
**Figure 6.** Flowchart of the procedure adopted to intertwine the derivation of classical and seismic parameters. Reddening maps 1–3 are the Drimmel et al. (2003) and the two flavors of the Amôres & Lépine (2005).

(A color version of this figure is available in the online journal.)

that, on average, the parameters derived in the two cases agree. The KIC magnitudes are affected by color-dependent zero-point offsets that are corrected according to Pinsonneault et al. (2012). Fortunately, the American Association of Variable Star Observers (AAVSO) Photometric All-Sky Survey (APASS) offers an independent source of photometry to check the soundness of the results obtained using the KIC corrected photometry. We use the latest APASS Data Release (DR7),

which covers 97% of the sky in the magnitude range 10–17 in the Johnson $BV$ and Sloan $g'r'i'$ filters. The advantage of implementing three different optical combinations in the IRFM is that the results in the Johnson–2MASS system are well standardized and much tested (Casagrande et al. 2010, 2012), while Sloan–2MASS allows us to check the consistency of the results obtained with the corrected KIC photometry plus 2MASS. The comparison among the three systems also

helps us asses the reliability of the results and the overall error budget (see also Section 3.7 and Figure 10). We stress here that optical broadband photometry is preferable to Strömgren for the IRFM since comparably little flux is encompassed within the intermediate bandwidth of the Strömgren system (which is almost entirely covered by our broadband photometry anyway). Furthermore, Strömgren bands are designed to be more sensitive to both log $g$ and [Fe/H], which would make the IRFM estimates more dependent upon those parameters.

### 3.2. Metallicities

Strömgren photometry is designed to effectively distinguish between dwarfs and giants and to provide reliable metallicity estimates in late-type stars (e.g., Önehag et al. 2009; Árnadóttir et al. 2010 and references therein). Much of the past literature has focused on metallicity calibrations for dwarf stars (e.g., Olsen 1984; Schuster & Nissen 1989; Haywood 2002; Nordström et al. 2004; Twarog et al. 2007; Casagrande et al. 2011), while considerably less attention has been devoted to giants. Most of the studies involving giants focused on the metal-poor regime (e.g., Faria et al. 2007; Calamida et al. 2007; Aden 2011), and the only calibrations extending up to the solar metallicity are essentially those of Grebel & Richtler (1992) and Hilker (2000).

We have already derived a metallicity calibration for dwarfs and subgiants in Casagrande et al. (2011), and here we extend it to giants. All calibrating stars in the metal-poor regime have Strömgren photometry from the extensive work of Grundahl et al. (1998, 2000, 2002), from which we cross-match stars with measured [Fe/H] in the following monometallic[20] globular clusters: NGC 6341 (M92, [Fe/H] = −2.64; Roederer & Sneden 2011), NGC 6397 ([Fe/H] = −2.10; Lind et al. 2011), NGC 6205 (M13, [Fe/H] = −1.58; Sneden et al. 2004), NGC 288 ([Fe/H] = −1.22; Carretta et al. 2009), NGC 6838 (M71, [Fe/H] = −0.82; Carretta et al. 2009), NGC 104 (47 Tuc, [Fe/H] = −0.75; Carretta et al. 2009). In the metal-rich regime we use our own Strömgren photometry, with single-member, seismic giants in the solar metallicity open cluster NGC 6819 (Stello et al. 2011) plus seven field giants we have in common with the spectroscopic sample of Thygesen et al. (2012). Altogether, our Strömgren metallicity sample of giants comprises 199 stars. We take reddening values for stars in globular clusters from the latest version of the Harris (1996) catalog.[21] This provides robust estimates, given that the majority of them have very low $E(B - V)$ and the absence of any substantial differential reddening (even for NGC 6397 and NGC 6838, which suffer from somewhat higher extinction; see Milone et al. 2012a). For NGC 6819 we adopted $E(B - V) = 0.14$, while for the remaining field giants reddening is estimated in much the same way as for our other *Kepler* targets (see Section 3.3).

We tested different functional forms relating Strömgren colors[22] to [Fe/H]. Instead of including all possible combinations of indices in some high-order polynomial, we started with a simple multilinear dependence on the three Strömgren indices and introduced mixed and higher-order terms after verifying that
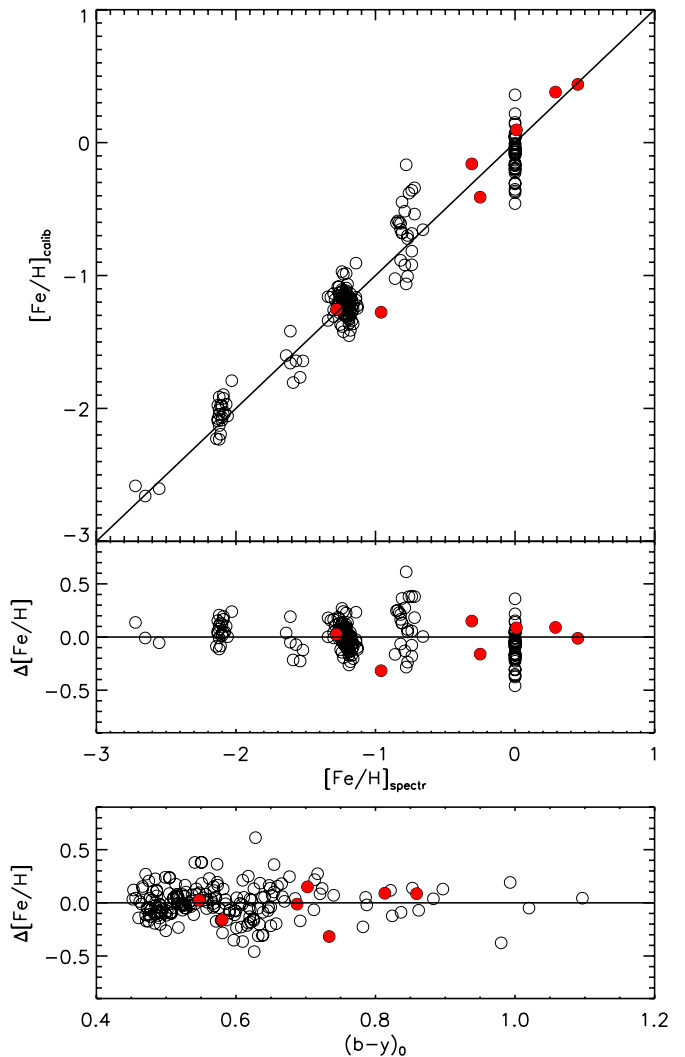
---

[20] For M92, Roederer & Sneden (2011) found that red giants are chemically homogeneous at the level of 0.07–0.16dex, although large nonhomogeneity in neutron capture elements is disputed (Cohen 2011).

[21] http://www.physics.mcmaster.ca/Globular.html

[22] In the following, we will refer to $c_1$, $m_1$, and $b-y$ with the implicit understanding that when deriving metallicities, these indices must first be dereddened.



**Figure 7.** Top: spectroscopic vs. photometric metallicities obtained using the calibration presented in Section 3.2 for giants. Open circles are giants in clusters, while filled circles are field giants from Thygesen et al. (2012). Middle: the same as above, but showing residuals (photometric minus spectroscopic). Bottom: the same as in the middle panel, but as a function of dereddened $(b − y)$, which is a proxy of the effective temperature.

(A color version of this figure is available in the online journal.)

they improved the residuals. The form adopted is the following:

$$
\begin{aligned}
[\text{Fe/H}] = &-9.037(b - y) + 4.875c_1 + 17.187m_1 \\
&+ 3.672(b - y)c_1 - 9.430(b - y)m_1 \\
&- 12.303c_1^2 - 17.405m_1^2 + 6.159(b - y)^2 \\
&+ 12.917m_1^3 - 0.972,
\end{aligned}
\tag{4}
$$

which applies to giants with $0.45 \leqslant (b - y) \leqslant 1.10$, $0.08 \leqslant m_1 \leqslant 0.92$, $0.08 \leqslant c_1 \leqslant 0.59$, and $-2.6 \lesssim [\text{Fe/H}] \lesssim 0.5$ dex, with a standard deviation of 0.15 dex (Figure 7). Notice that we apply this calibration to all our giants (see Figure 17), while for dwarfs we rely on the similar calibration derived in Casagrande et al. (2011). As there are no calibration giants above [Fe/H] $\simeq$ 0.5 dex in the sample, if a star has a metallicity higher than this value or if its Strömgren indices fall outside of the applicability range determined above, we flag the measurement. This and the *uvby* photometric quality flag determined in Section 2.3 identify stars with the most reliable metallicities based on the Strömgren photometry. As a result, these flags
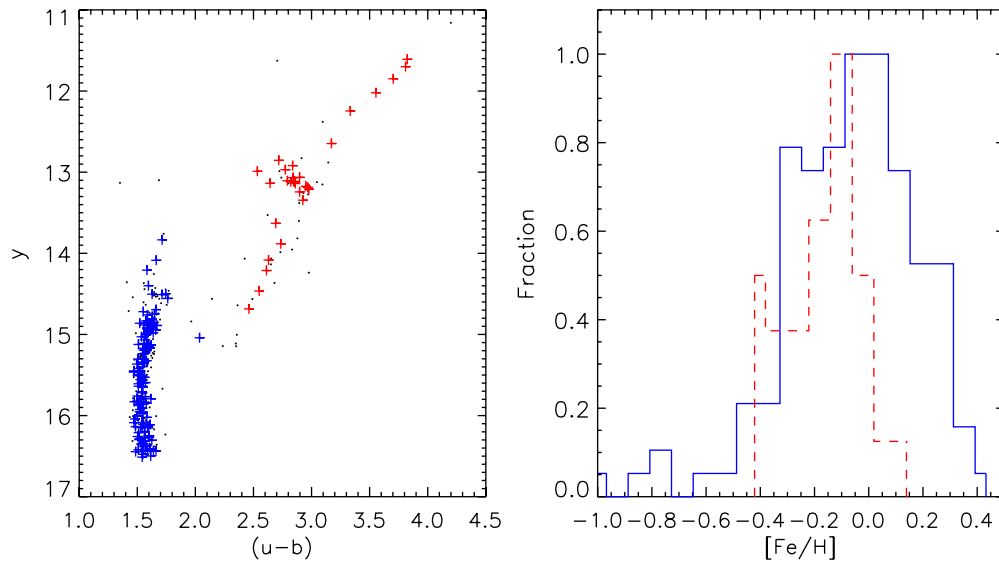
**Figure 8.** Left: NGC 6819 color–magnitude diagram. Only single stars having radial velocity membership probabilities higher than 80% in Hole et al. (2009) are shown. Highlighted in red (blue) are giant (main-sequence) stars within $\simeq 7$ arcmin from the cluster center and with photometric errors below the ridgelines of Figure 4. Right: Strömgren metallicity histogram for the same dwarfs (continuous line) and giants (dashed line) highlighted in the left panel. The difference between the peaks of the metallicity distributions of dwarfs and giants (0.08 dex) has been corrected as explained in Section 3.2.

(A color version of this figure is available in the online journal.)

help us diagnose cases where stars with slightly unusual colors might return unrealistic metallicities.

Equation (4) differs from the functional form often used for giants; in particular, it includes a dependence on the $c_1$ index, which was not measured in many past works (the low flux in the $u$ band of relatively faint giants being too time-consuming to measure with photoelectric photometers). The standard deviation of our giant calibration is somewhat larger than for dwarfs ($\lesssim 0.1$ dex; Casagrande et al. 2011); this could partly originate from the fact that the calibration sample already carries some uncertainty in the adopted reddening values. As we see later, the typical reddening uncertainty is around $\sigma_{E(B-V)} = 0.02$, and this affects Strömgren metallicities by 0.09 dex on average. We thus take a conservative approach and quadratically sum this error to the above standard deviation, yielding a typical uncertainty of 0.17 dex for our metallicities. As the SAGA survey continues, we plan to improve and expand the above calibration with a larger and more uniform sample of giants having spectroscopic metallicities and abundances. In addition, Strömgren indices are known to be sensitive to more than just [Fe/H] in cool stars, and we plan to investigate this effect as well (e.g., Yong et al. 2008; Casagrande et al. 2011; Carretta et al. 2011).

The open cluster NGC 6819 offers the possibility to check the consistency between the metallicity calibration derived here for giants and that used for dwarfs in our previous analysis of the solar neighborhood (Casagrande et al. 2011), as well as for the few dwarfs present in this sample (see Figure 17). We identify dwarfs and giants in NGC 6819 by using the same procedure for both: we cross-match our Strömgren observations with the radial velocity catalog of Hole et al. (2009) and retain only single stars with cluster membership probability $>80\%$ and within $\simeq 7$ arcmin of the center of the cluster. Note that with this procedure, some of the cluster giants are not the same as used for our metallicity calibration, which had more secure seismic membership (Stello et al. 2011). The comparison in Figure 8 shows that metallicities of dwarfs and giants agree on average. However, two things should be noted. First, the

dwarfs exhibit a larger scatter, which is partly due to the larger photometric errors at fainter magnitudes and because the sensitivity of Strömgren indices to metallicity is reduced for warmer dwarfs compared to giants. Second, the peak of the two metallicity distributions differs by some 0.08 dex, with the giants being more metal-poor. Such an offset is not surprising, given that there might be a difference in the effective temperatures underlying the spectroscopic measurements used to build the dwarf (Casagrande et al. 2011) and the giant (derived here) metallicity calibrations. In fact, spectroscopic [Fe/H] in giants are often derived using different flavors of the Alonso et al. (1999) $T_{\rm eff}$ scale. This is about 100 K cooler than the one now preferred for dwarfs and giants (Casagrande et al. 2010, 2014). Since the metallicity calibration for dwarfs used spectroscopic metallicities based on a $T_{\rm eff}$ scale hotter than Alonso et al. (1999), the aforementioned 100 K difference in giants can easily account for the metallicity offset found here. Obviously, this zero-point difference can be corrected, and for convenience the last term in Equation (4) is already shifted by this amount (a later comparison done in Figure 16 confirms that with such a correction giants in the cluster indeed have solar metallicity).

One could argue that [Fe/H] should be slightly *lower* in dwarfs than giants belonging to the same stellar population because of the settling of heavy elements in main-sequence stars (e.g., Korn et al. 2007). However, because of the uncertainties discussed above and the relatively young age of the cluster ($\simeq 2.5$ Gyr; e.g., Yang et al. 2013; Jeffries et al. 2013; Sandquist et al. 2013), we believe this effect to be well within the uncertainties of our photometric metallicities.

### 3.3. Reddening

Even though the Galactic stripe observed for this work avoids excessively high values of color excess, nonnegligible reddening is still present and must be corrected for before we can use photometry to derive stellar parameters. We did a comparison between the color excess reported in the KIC for over 13 million objects and $E(B - V)$ derived at their same positions in the sky from the Schlegel et al. (1998) map (Figure 1). This revealed

that that extinction in the KIC lacks fine structure. This is not surprising since reddening in the KIC is estimated using a simple dust model that assumes a smooth exponential disk with a scale height of 150 pc and 1 mag of attenuation in the $V$ band per kiloparsec in the plane. Thus, color excess from the KIC is used only as a starting point in our iterative scheme (Section 3).

Because we derive distances for all our stars, we can use three-dimensional extinction models. We use two different ones: those of Drimmel et al. (2003) and Amôres & Lépine (2005). Drimmel's map is based on a dust distribution model applied to three Galactic density components and rescaled to recover the observed far-infrared emission as observed by the *COBE* satellite. The Amôres & Lépine (2005) map is based on the measured gas density distribution and translated into extinction under the assumption that gas and dust are well mixed. This model is available for two configurations, one assuming that the Galaxy is axisymmetric and one taking into account the spiral structure of the Galaxy.

The scale of the geometrical components used in all of these models of the Galaxy is poorly known, and therefore, the spatial distribution of extinction is uncertain. In fact, all these models suggest that rescaling factors can be used, should these be needed to satisfy reddening constraints in particular lines of sight.

Once again, the open cluster NGC 6819 offers an important calibration point. It is located at the base of our Galactic stripe (Figure 1), and its giants are in the same magnitude range as the other *Kepler* giants with detected oscillations (Figure 8), thus broadly representing the typical mean distance probed in our investigation (see also Figure 2). Its reddening is also well constrained: we adopt $E(B - V) = 0.14$ from Bragaglia et al. (2001), which falls within the 0.12–0.16 range of values found using different methods (e.g., Rosvick & Vandenberg 1998; Jeffries et al. 2013). Using our Strömgren photometry, we apply the empirical method described in Milone et al. (2012b) to derive a $14 \times 14$ arcmin map of differential reddening centered on the cluster, which shows spatial variations of order $\pm 0.02$ mag. This is consistent with the result of Platais et al. (2013) and reassures us that even at the lowest latitudes of our sample, differential reddening, while present, is not a major concern for our analysis.

We thus rescale the Drimmel et al. (2003) and Amôres & Lépine (2005) models to have $E(B - V) = 0.14$ at the position and distance of NGC 6819 (2.4 kpc from isochrone fitting; Yang et al. 2013) and use these recalibrated maps to estimate reddening for all our stars. Incidentally, we note that after this rescaling, the axisymmetric and the spiral model of Amôres & Lépine (2005) are virtually identical (always to better than 0.01 mag) over the Galactic coordinates and distances covered in this investigation. For consistency we perform our analysis using the three models, but in practice we will always refer to both Drimmel et al. (2003) and Amôres & Lépine (2005) with the implicit assumption that the two flavors of the latter have been compared and that no substantial difference is found in the parameters derived.

With respect to extinction models, 2MASS photometry offers an alternative and empirical way to gauge the reddening. To this end, we select from the 2MASS Point Source Catalog (Skrutskie et al. 2006) a region roughly centered at the same longitude of our Galactic stripe, i.e., $|l - 72°.5| < \pm 2°.5$, and we retain only targets having good infrared photometric flags[23] (i.e., quality "AAA" and blend "111"). Figure 9 shows the

$J - K_S$ versus $K_S$ plane for sources at four different latitudes. At the highest latitudes, where reddening is lowest, three main features are obvious: (1) the bluemost overdensity, which mainly comprises main-sequence and turnoff stars, (2) the central one mostly made up of giants, and (3) the rightmost and fainter group of cool dwarfs. Moving to lower Galactic latitudes, these features blur, and a prominent puff of stars appears at the redmost colors. Reddening is indeed the main factor in shaping these morphological changes across the panels, as both age and metallicity play a minor role in the near-infrared color–magnitude diagram. This is shown with isochrones in the top right panel of Figure 9. The main position of the red giant population is always located at approximately the same color $J - K_S \simeq 0.6$–0.7, regardless of the age (1 and 10 Gyr) and metallicity ([Fe/H] $\simeq -1$ and $\sim 0$) of the underlying population. We note that the isochrones shown here span a range considerably larger than the mean variation measured in this part of the disk. Thus, we can turn this argument around to derive the value of reddening at each Galactic latitude such that the red giant population is restored to the same $J - K_S$. This can be used to verify the adopted Galaxy model reddening maps.

From this 2MASS stripe, we sample Galactic latitudes between $7°$ and $20°$ at constant steps of either $0°.5$ or $1°$ (to check different resolution effects) and each time derive the corresponding $J - K_S$ versus $K_S$ diagram. We consider only stars having apparent magnitudes $6 < K_S < 11$. This choice is representative of the magnitudes, and hence distances, of the bulk of our *Kepler* giants, and it also minimizes contamination from dwarfs (the reddest overdensity of dwarfs in the left panels of Figure 9 starts at somewhat fainter magnitudes). We then sample the reddening space in the range $0 \leqslant E(B - V) \leqslant 0.4$ in steps of 0.01, each time dereddening the color-apparent magnitude diagram at the value of $E(B - V)$ considered. For the sake of our analysis each color-apparent magnitude diagram is reduced to a histogram of the relative number of stars as a function of $J - K_S$ color. The purpose is to derive a reddening map whose values are differential with respect to a reference value. Here the histogram at the highest latitude sampled is taken as reference, and hence, its color magnitude diagram is uncorrected for reddening, even if it could have a nonzero value of $E(B - V)$. All histograms derived at lower latitudes and for different values of $E(B - V)$ are benchmarked against this. Then, at each latitude we find the value of $E(B - V)$ that best matches the reference histogram in the color range $0.5 \leqslant J - K_S \leqslant 1.5$. These last values are set somewhat arbitrarily to avoid the inclusion of the age-sensitive turnoff population and to probe the population of red giants well enough. We verified that changing these limits within reasonable values ($\simeq \pm 0.1$ mag) does not severely affect our results. This differential approach can then be put on an absolute scale should the value of reddening be known in one of the fields: this is indeed the case at the location of the open cluster. All $E(B - V)$ solutions are thus shifted by the amount needed to pass through the reddening of NGC 6819 at $b = 8°.5$. As already mentioned, we sample Galactic latitudes in steps of both $0°.5$ and $1°$ to check whether our results depend on the adopted binning: the agreement is quite reassuring, always within a few hundredths of a magnitude, although values of $E(B - V)$ derived sampling each $0°.5$ appear to be more noisy. This is expected because of the smaller number of stars when using smaller bins, especially toward the highest latitudes. From this scatter we estimate $\sigma_{E(B-V)} = 0.02$ on average for the population *as a whole*. The reddening maps built with such a procedure have a rather coarse resolution but benefit from being

_____

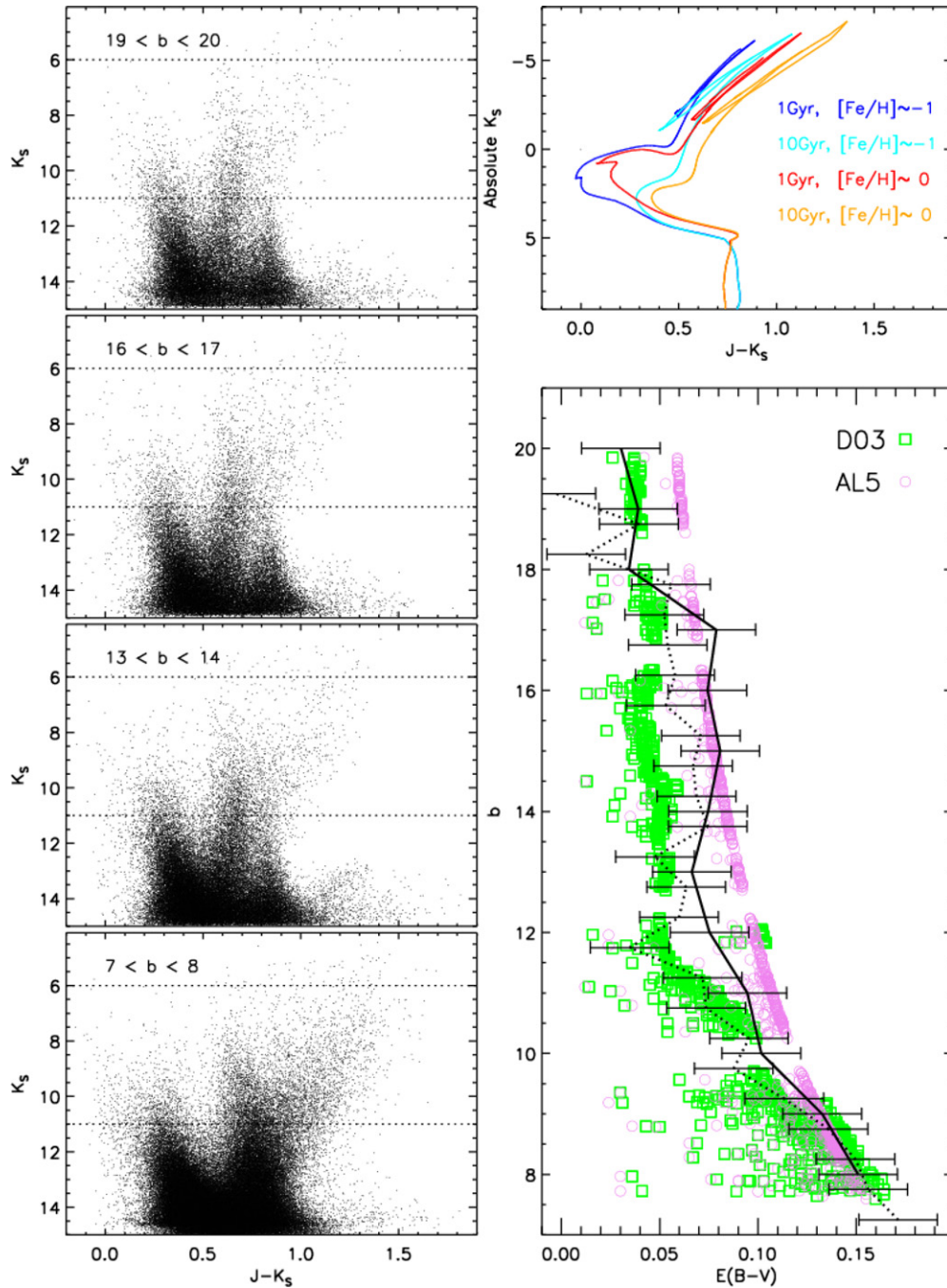[23] http://www.ipac.caltech.edu/2mass/releases/allsky/doc/sec2_2a.html

**Figure 9.** Left: observed $J - K_S$ vs. $K_S$ diagram for stars with good 2MASS photometry at selected intervals in Galactic latitude $b$ and with longitude $|l - 72°.5| < 2°.5$. Dotted horizontal lines indicate the $K_S$ magnitude range used to empirically derive reddening (see the text for details). Top right: BaSTI isochrones in the 2MASS system for two values of metallicity and age (Pietrinferni et al. 2004). Bottom right: reddening derived using the procedure described in Section 3.3, sampling the 2MASS color-apparent magnitude diagram each 0°.5 (dotted line) or 1° (continuous lines) after scaling to the $E(B - V)$ of NGC 6819. Open circles and squares are reddening values derived for our *Kepler* stars using the Amôres & Lépine 2005 (AL05) and Drimmel et al. 2003 (D03) maps.

(A color version of this figure is available in the online journal.)

empirical and completely independent from both Drimmel et al. (2003) and Amôres & Lépine (2005).

The overall level of agreement between different maps and our empirical method is quite comforting provided that NGC 6819 is used as an anchor point and gives us confidence that our parameters are not severely affected by reddening. Note that all our stellar parameters are derived using both the Drimmel et al. (2003) and Amôres & Lépine (2005) maps, while the empirical method developed here does not contain any distance information on single stars. However, besides validating the

adopted extinction maps, the empirical method allows us to estimate the average uncertainty in reddening, at the level of 0.02 mag, and thus to assess the robustness of the stellar parameters we derive in the presence of this uncertainty.

### 3.4. Global Asteroseismic Parameters and Evolutionary Phase Classification

Stellar oscillations driven by surface convection, such as those observed in the Sun and red giants, are visible in the power

spectrum of time series photometry as a series of Lorentzian-shaped peaks whose peak height is modulated in frequency by a Gaussian-like envelope (e.g., Chaplin & Miglio 2013). Two quantities can be readily extracted from this oscillation pattern: the average separation between peaks of the same angular degree and consecutive radial order, the large-frequency separation $\Delta\nu$, and the frequency of maximum amplitude $\nu_{max}$ (e.g., Ulrich 1986; Brown et al. 1991). These global asteroseismic parameters have been determined for the full sample of giants that we consider here. A few dwarfs are also present in the sample, and their classification comes from Chaplin et al. (2014).

Provided that the time resolution and quality of the observations are good enough, additional information can be extracted from the power spectrum of red giants thanks to the presence of *mixed modes* (see, e.g., Bedding 2011 for a review). These oscillations have an acoustic character in the outer layers while behaving like gravity waves in the deep interior of a star, providing unique information about the stellar core. Stars evolving along the RGB, burning hydrogen in a shell around the inert helium core, are very difficult to distinguish from their helium-core-burning red clump (RC) counterparts by classical photometric and spectroscopic observations. However, RGB stars have a radiative core, while clump giants have a convective one. Measurement of the average spacing between mixed dipole modes clearly separates these stars into two distinct populations of giants (Bedding et al. 2011; Mosser et al. 2012).

We have analyzed *Kepler* long-cadence data (Jenkins et al. 2010) through Quarter 15 for all giants in our sample. About 30% of the sample has been observed continuously throughout the mission (with a maximum data set length of 1350 days), while 70% has more than 10 quarters of data available. Simple-aperture photometry (SAP) data were used for our analysis. Instrumental flux discontinuities were corrected by fitting linear functions to 5–10 day subsets before and after each discontinuity (see, e.g., García et al. 2011). Finally, for all time series a quadratic Savitzky–Golay filter (Savitzky & Golay 1964) was applied to remove additional variability due to stellar activity and instrumental effects. Because of the wide range of oscillation periods covered in our sample we used two different filters: for stars with oscillation periods >1 day we applied a 50 day filter, and for all remaining stars a 10 day filter was used.

We have classified the red giant stars into two main groups: those burning only hydrogen in a shell located on the RGB and those burning helium in the core in the RC. To distinguish these two groups, we looked for the seismic signature of the stellar core properties according to Bedding et al. (2011). Specifically, we measured the period spacing of the dipole modes following the approach by Stello et al. (2013). We were able to measure the period spacing and unambiguously classify 427 stars in this way (169 RGB and 258 RC). The remaining giant stars did not show a sufficient signal-to-noise ratio in the frequency power spectra to provide reliable classification.

To extract the global oscillation parameters $\Delta\nu$ and $\nu_{max}$, we have used the analysis pipeline described by Huber et al. (2009), which has been shown to agree well with other methods (Hekker et al. 2011a; Verner et al. 2011). Uncertainties for each parameter were determined through Monte Carlo simulations, as described in Huber et al. (2011). For each value we added in quadrature an uncertainty arising from the use of solar reference values to estimate stellar properties (Section 3.5). The final median uncertainties on $\Delta\nu$ and $\nu_{max}$ were 0.7% and 1.7%, reflecting the exquisite signal-to-noise ratio of the *Kepler* data.

### 3.5. Masses, Radii, and Distances

We have used grids of isochrones in combination with a Bayesian analysis that includes asteroseismic quantities to determine the stellar parameters of our sample. The reference isochrones are constructed from the noncanonical BaSTI models, which include core overshooting during the H-core-burning phase and do not consider mass loss. These isochrones have been computed explicitly for this work, while the publicly available[24] BaSTI grid assumes a Reimers (1975) mass loss parameter of either $\eta = 0.4$ or $\eta = 0.2$. The helium to metal enrichment ratio is fixed at $\Delta Y/\Delta Z = 1.45$, consistent with the value inferred from the broadening of the low main sequence (Casagrande et al. 2007) and from models of stellar nucleosynthesis and chemical evolution of the Galactic disk (e.g., Maeder 1992; Carigi & Peimbert 2008). A detailed account of the input physics of the models is given in Pietrinferni et al. (2004). We note that measurements of period spacings between mixed modes in clump stars observed by *Kepler* (Mosser et al. 2012) can only be reproduced if mixing beyond the formal Schwarzschild boundary of the He-burning convective core is included (Montalbán et al. 2013). In BaSTI models, this extra mixing is accounted for by including semiconvection during the He-core-burning phase.

The Bayesian analysis is performed as described in Serenelli et al. (2013). In summary, if **v** is a set of stellar parameters from models (e.g., mass, radius, metallicity, age, effective temperature) and $\mathcal{O}$ is the observed data, i.e., $\mathcal{O} \equiv (T_{eff}, \Delta\nu, \nu_{max}, [Fe/H])$, then according to Bayes' rule, the probability density function (pdf) of **v** given $\mathcal{O}$, i.e., the posterior pdf $p(\mathbf{v}|\mathcal{O})$, is given by

$$p(\mathbf{v}|\mathcal{O}) \propto p(\mathbf{v})\, p(\mathcal{O}|\mathbf{v}), \qquad (5)$$

where $p(\mathcal{O}|\mathbf{v})$ is the likelihood of $\mathcal{O}$ given **v** and $p(\mathbf{v})$ is the prior pdf of **v** and represents prior knowledge of these quantities. The likelihood is computed assuming errors in $\mathcal{O}$ follow Gaussian distributions.

To determine $p(\mathbf{v})$, we considered the following. The effective selection function of pulsating stars observed by *Kepler* is nontrivial. Therefore, we cannot characterize a prior probability of stellar properties based on the fact that the star is in the *Kepler* field. For this reason, we assume a flat prior in [Fe/H] and age including only a strict cut on the latter at 16 Gyr. For the prior in mass we assume a standard Salpeter initial mass function(IMF). In the cases where it is possible to measure the separation between mixed modes (see Section 3.4 above), the information obtained on the evolutionary phase of the star is also included as a (binary) prior such that only stellar models corresponding to the determined evolutionary phase are used in the analysis. When this information is not available, all models are considered, and stellar properties can suffer from large uncertainties because both the RGB and clump evolutionary phases have non-negligible likelihoods. Bimodal probability distributions could, in principle, arise in those cases, influencing the estimation of reliable properties for these stars.

Once the posterior pdf has been computed for a star, the posterior pdf of any stellar quantity $x$ can be simply obtained as

$$p(x|\mathcal{O}) = \int \delta(x(\mathbf{v}) - x) p(\mathbf{v}|\mathcal{O}) w_v d^3 v, \qquad (6)$$

where $w_v$ accounts for the volume of parameter space occupied by an isochrone point characterized by **v** (see Appendix A in Casagrande et al. 2011).

---

[24] http://www.oa-teramo.inaf.it/BASTI

The computation of the likelihood function in Equation (5) requires determination of theoretical values for $\Delta\nu$ and $\nu_{max}$. Those can be derived from the adopted grid of isochrones due to scaling relations. To a good approximation, $\Delta\nu$ scales with the mean density of the star (Ulrich 1986), while $\nu_{max}$ is related to the surface properties (Brown et al. 1991; Kjeldsen & Bedding 1995). From the solar values, two asteroseismic scaling relations can be written (e.g., Stello et al. 2009; Miglio et al. 2009):

$$\frac{\Delta\nu}{\Delta\nu_\odot} \simeq \frac{(M/M_\odot)^{0.5}(T_{eff}/T_{eff,\odot})^3}{(L/L_\odot)^{0.75}}, \qquad (7)$$

$$\frac{\nu_{max}}{\nu_{max_\odot}} \simeq \frac{M/M_\odot(T_{eff}/T_{eff,\odot})^{3.5}}{L/L_\odot}, \qquad (8)$$

where $\Delta\nu_\odot = 135.1\ \mu Hz$ and $\nu_{max_\odot} = 3090\ \mu Hz$ are the values observed in the Sun for the adopted method in this paper (Huber et al. 2011). Using parallaxes and interferometric measurements, radii determined using these scaling relations have been shown to be accurate to better than 5% in dwarfs (e.g., Silva Aguirre et al. 2012; Huber et al. 2012; White et al. 2013). Further tests on the reliability of the scaling relations are summarized in Miglio et al. (2013b).

Having now all the information needed to compute both the prior and the likelihood, the pdf for the relevant parameters of each star can be computed, including masses and radii. Further, precise distances can also be determined by scaling these radii with the angular diameters obtained via the IRFM. As summarized in Section 3, stellar parameters have been determined via an iterative process coupling the photometric and asteroseismic parameters. In every iteration we used the median and 68% confidence levels of the pdf to determine the central value and (asymmetric) uncertainty of each quantity. We call these errors "formal uncertainties," and we explore the effect of using different stellar models and pipelines on the error budget later in Section 3.7.

### 3.6. Unresolved Binary Contamination

In principle, the presence of undetected binaries is important since, should this happen, the colors measured for a star would also carry the contribution from its companion, thus affecting all photometric quantities derived and subsequently used for the seismic analysis (Sections 3.1–3.5). Fortunately, our sample comprises mostly RGB stars, for which the fraction of similar luminosity binaries is extremely rare (∼1%; e.g., Nataf et al. 2012). Moving to lower-mass companions, the fraction of spectroscopic binaries among K and M giants ranges from ∼6% to ∼30%, where observational difficulties, as well as accounting for selection effects, prevent better estimates (e.g., Frankowski et al. 2009).

A number of important photometric flags are available for all seismic stars used in this work, 96% of our targets having the best possible 2MASS pedigree:[23] quality flag AAA, blend flag 111 (meaning one component is fit to the source), and contamination and confusion flag 000 (meaning the source is unaffected by known artifacts) in all three infrared bands. The remaining 4% of stars with one or more flags set differently from above usually have larger photometric errors that are thus accounted for in our Monte Carlo, naturally resulting in larger error bars (see Section 3.7).

Synthetic photometry offers a qualitative way of assessing the level of contamination expected from a companion. From the MARCS library of synthetic spectra (Gustafsson et al. 2008)

we assume $\log g = 2.5$, [Fe/H] = 0, and $T_{eff} = 4750$ K for a typical giant to which we assign a radius of $10\ R_\odot$. For the secondary, we consider two representative cases: in one the companion is identical to the Sun, while in the other it is an M dwarf ($\log g = 5.0$, [Fe/H] = 0, and $T_{eff} = 4000$) with radius $0.7\ R_\odot$. Assuming that both binary components randomly sample the IMF, this last case is likely to be the most probable, given that by number M dwarfs are the dominant stellar population in the Galaxy (e.g., Reid & Hawley 2005).

As expected, the flux contribution of an M dwarf is entirely negligible compared to a giant: optical and infrared colors are affected by 1 to 4 mmag, thus having no impact on the IRFM. Strömgren $b-y$, $m_1$, and $c_1$ indices are even less affected, a few parts over 10,000 at most. In the presence of a solar companion, the effect is between 0.01 and 0.02 mag in both broadband and Strömgren colors, with only moderate impact on the photometric parameters derived. Our conservative error bars account for any such uncertainty. Of course, other combinations in the ratio of the primary to secondary effective temperature and radius are possible, but the two cases explored above are representative of the most common scenarios and give us confidence that binary contamination, when present, barely affects our parameters.

*Kepler* data provide an additional tool to quantify binary contamination in the sample. In addition to $\Delta\nu$ and $\nu_{max}$ the asteroseismic analysis described in Section 3.4 yielded estimates of the global oscillation amplitude, which is well known to correlate with stellar properties (see, e.g., Corsaro et al. 2013). Any near equal-mass binary companion would result in a second oscillation signal with nearly equal frequency, causing a significant dilution of the observed amplitude. A second oscillation signal is observed for only five stars in our sample, with estimated luminosity ratios ranging from ≃0.4 to 0.8. These stars have been flagged in the analysis.

### 3.7. Total Error Budget

For all nine possible different combinations of broadband photometric systems (three) and reddening maps (three), we derive both self-consistent parameters and uncertainties. For each star, uncertainties in the physical parameters derived from the IRFM (effective temperature, bolometric flux, and angular diameter) are computed in a fashion very similar to Casagrande et al. (2010). First, a Monte Carlo is run to account for random photometric errors, according to the set of filters used in the IRFM. We use uncertainties quoted for each band in 2MASS ($JHK_S$) and APASS ($BV$ and $g'r'i'$); no star-by-star uncertainties are reported in the KIC ($griz$), and we thus use a constant uncertainty of 0.02 mag in each filter (Figure 4 in Brown et al. 2011).

For reddening we explore a systematic variation of $E(B-V) = \pm0.02$ with respect to the values adopted from each map. This variation in reddening is also used to compute by how much the Strömgren metallicities change. As already mentioned (Section 3.2), this metallicity variation is added quadratically to the scatter of the [Fe/H] calibration, returning a typical global uncertainty of 0.17 dex. This is used to compute how much the parameters derived via the IRFM vary, although we recall once again that the IRFM is only mildly sensitive to the input [Fe/H]. In this way, reddening enters our errors twice, both in the broadband colors and in the metallicities used in the IRFM; the choice to maximize its effect is motivated by the fact that we aim to derive realistic and conservative uncertainties. Finally, the effect of varying $\log g$ by 0.1 dex is included: the precision of seismic gravities is actually much higher (≲0.03 dex;

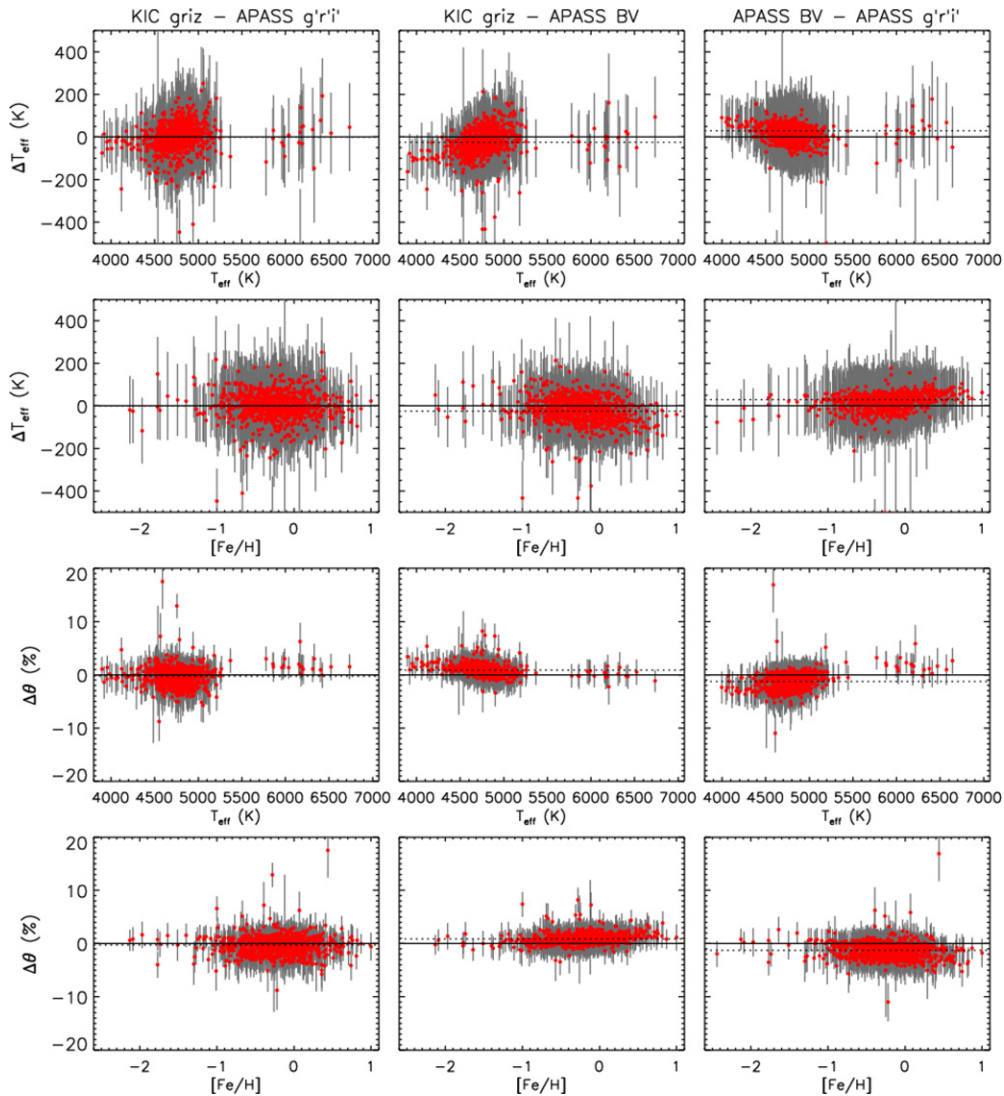**Figure 10.** Comparison between $T_{eff}$ (first and second rows) and $\theta$ (third and fourth rows) derived implementing different optical photometric systems in the IRFM (first, second, and third columns), with corresponding error bars. In all instances, the same reddening map is used (see discussion in Section 3.7), although adopting a different one barely changes this comparison. Dotted lines represent the median differences.

(A color version of this figure is available in the online journal.)

e.g., Gai et al. 2011; Thygesen et al. 2012; Morel & Miglio 2012), but the IRFM is so largely insensitive to $\log g$ that even this very conservative uncertainty has virtually no effect on the error budget. All uncertainties listed above (Monte Carlo, reddening, metallicity, and gravity) are added quadratically and are further increased by 1.0% and 0.7% for bolometric fluxes and angular diameters and 20 K for $T_{eff}$ to account for our uncertainty in the absolute zero point of those scales (Casagrande et al. 2010). We recall that the effective temperature, bolometric flux, and angular diameter of each star are usually derived using three different implementations of the IRFM ($grizJHK_S$, $BVJHK_S$, and $g'r'i'JHK_S$): a comparison among those is shown in Figure 10. For the sake of the latter, the same reddening map is used, although in some cases distances change depending on the filter combination used in the IRFM, and thus, the values derived for $E(B-V)$ change as well, even when using the same map. Metallicities are derived from Strömgren colors only, although for the reason just explained $E(B-V)$ might be slightly different among the three implementations of the IRFM. Fortunately, this reddening variation within the same map has

virtually no effect on [Fe/H], often being null and typically well below 0.01 dex.

Having now three different sets of $\mathcal{F}_{Bol}$, $\theta$, $T_{eff}$, and [Fe/H], each with its own error, we can combine this information by using the weighted average. The values derived in this way for a given reddening map are dubbed "consolidated" parameters. In the ideal case, different filter combinations should all return the same values for a given reddening map. Within the uncertainties, this is indeed the case (Figure 10). The weighted sample standard deviation, which measures the overdispersion of the weighted averaged parameters, tells us their internal consistency: reassuringly, this is very close to the values obtained with the Monte Carlo for each implementation of the IRFM. To obtain the final global errors, we quadratically add the weighted sample standard deviation to the errors computed above for each star. Their median values are 82 K in $T_{eff}$, 0.17 dex in [Fe/H], 2% in angular diameters, and 5% in bolometric fluxes.

The procedure outlined above is repeated for each reddening map. A comparison between the results obtained adopting Drimmel et al. (2003) or Amôres & Lépine (2005) is shown
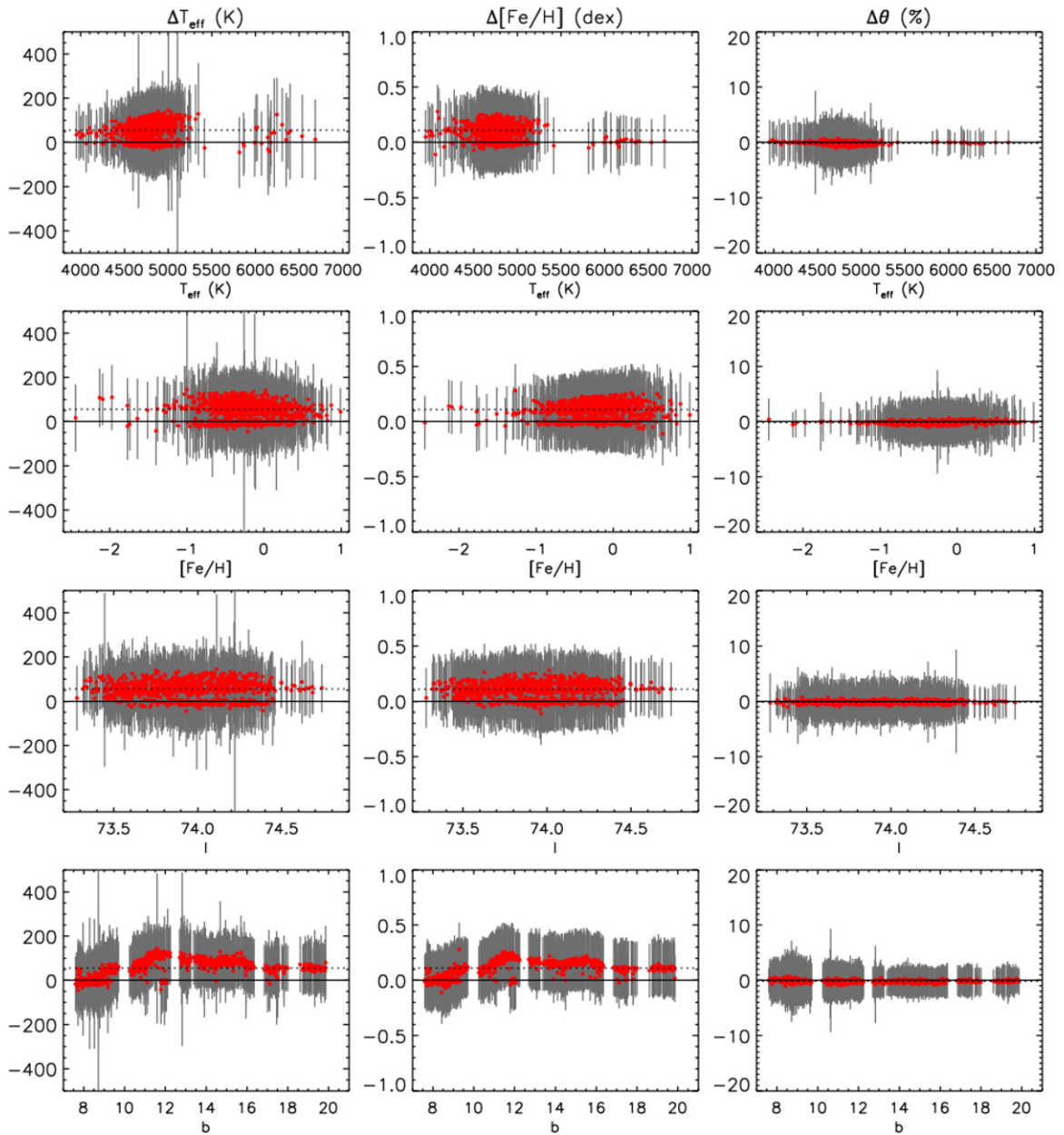
**Figure 11.** Comparison between the consolidated set of effective temperatures (first column), metallicities (second column), and angular diameters (third column) derived using two different reddening maps (Amôres & Lépine 2005 minus Drimmel et al. 2003). Stars showing almost no difference are those located at Galactic latitudes $b \simeq 8.5$, where both maps are anchored at the $E(B - V)$ of NGC 6819. The dotted line is the median difference.

(A color version of this figure is available in the online journal.)

in Figure 11; as expected from our conservative approach in estimating realistic error bars, results always agree within the uncertainties. Median differences are relatively small and rather uniform, with no particular dependence on Galactic coordinates, especially for latitudes above $10°$. At smaller $b$, the agreement is much better and reflects our use of the reddening of NGC 6819 as an anchor point.

These consolidated parameters are used once again in the seismic scheme described in Section 3.5 to derive a final set of radii, distances, and masses with median formal uncertainties of order 2%, 3%, and 5%, respectively. These values are of the same order as those found in other asteroseismic studies when reliable information on stellar effective temperatures and metallicities is available. In particular, errors in masses and radii are positively correlated, and this leads to very small errors in

gravities (e.g., Gai et al. 2011; Creevey et al. 2013; Chaplin et al. 2014). Nevertheless, it should be kept in mind that as of yet, there are only a few empirical tests of the accuracy of the scaling relations when applied to giants (see also the discussion in Section 3.5), and modest systematic errors are thus possible (Miglio et al. 2012). However, the clear separation of the first and secondary clumps in our data gives confidence on the internal precision of our gravities. Figure 12 extends the comparison between different reddening maps to seismic quantities, where stars with different seismic classification are highlighted in colors; differences are also always within the error bars in this case. We also explore the impact on the derived stellar parameters of varying the input physics in our reference BaSTI grid of isochrones. We test the effect of switching on mass loss with high efficiency ($\eta = 0.4$) during
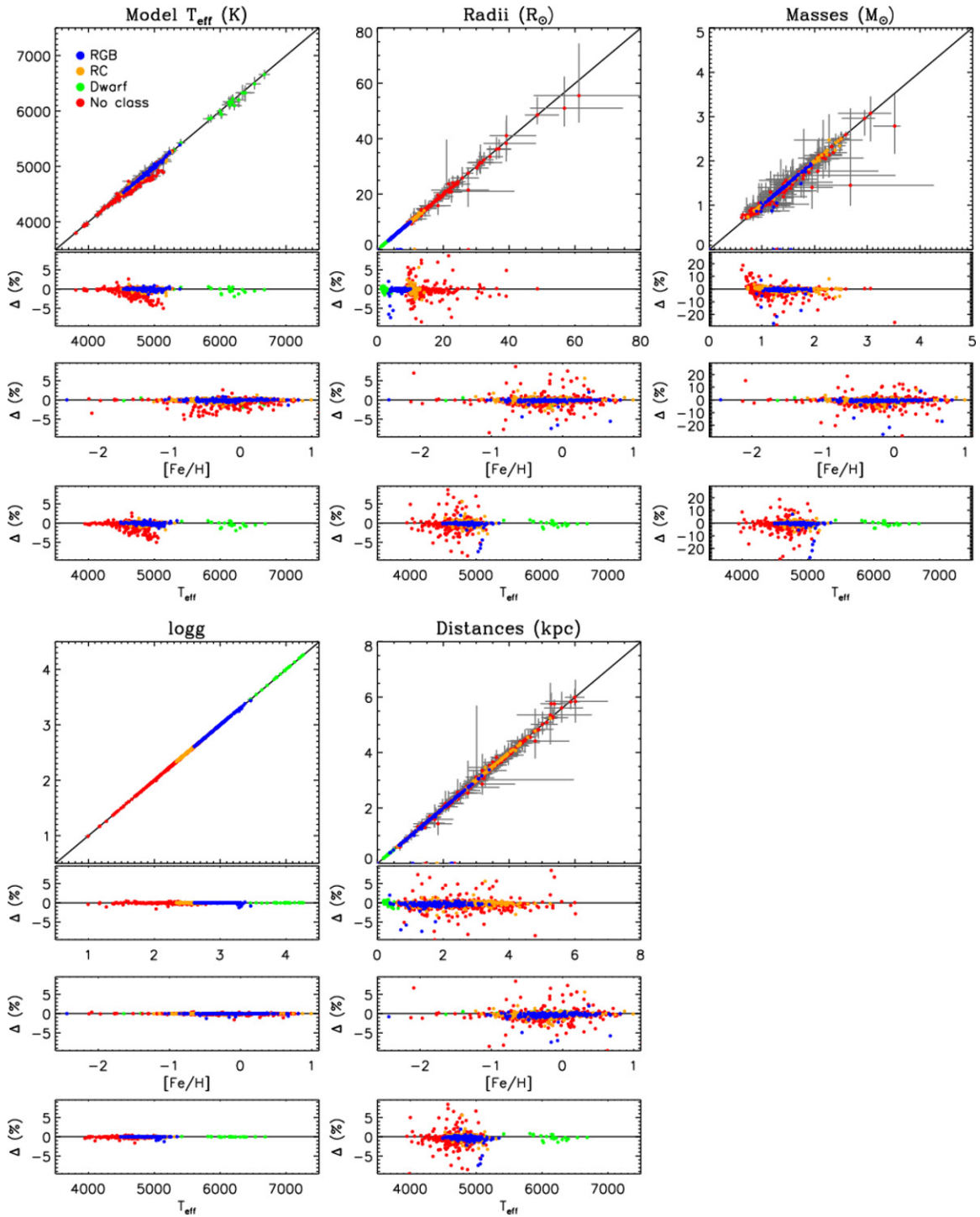
**Figure 12.** Difference in the classical plus seismic quantities derived when using the Amôres & Lépine (2005; horizontal axis) and Drimmel et al. (2003; vertical axis) reddening maps. The fractional difference is shown as a function of the parameter investigated, as well as of the consolidated $T_{\rm eff}$ and [Fe/H]. Different colors identify stars with different seismic classification.

(A color version of this figure is available in the online journal.)

the evolution, finding that the formal uncertainties quoted above are more than two times larger than the median difference in the derived stellar parameters. Similarly, isochrones with no core overshoot during the main-sequence phase give differences about 10 times smaller than the formal uncertainties. Hence, these effects have overall little impact on the parameters derived here (although this would not always be the case for stellar ages).

To account for systematics arising from different evolutionary codes and implementation of input physics, we derived Bayesian stellar parameters using an extension of the grid of models presented in Serenelli et al. (2013), constructed using the GARching STellar Evolution Code (GARSTEC; Weiss & Schlattl 2008) and covering a mass and metallicity range of $0.6 \leqslant M_\odot \leqslant 3.0$ and $-3.0 \leqslant$ [Fe/H] $\leqslant +0.5$. Similarly, we determined stellar properties from BaSTI evolutionary tracks using the Monte
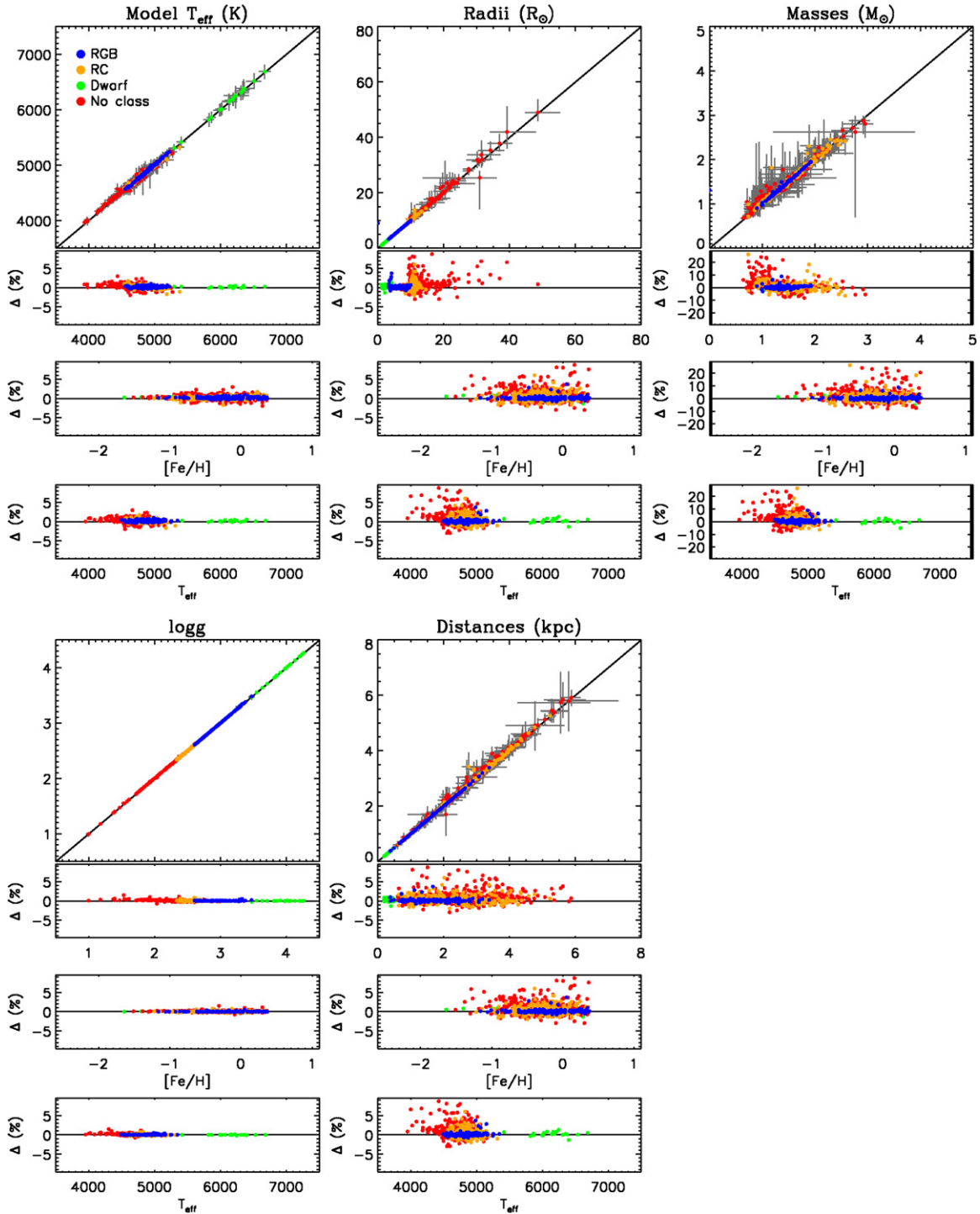
**Figure 13.** Same as Figure 12, but comparing the effect of using a Bayesian (horizontal) or a Monte Carlo (vertical) scheme with the BaSTI models to derive seismic parameters. The same reddening map is assumed in both cases.

(A color version of this figure is available in the online journal.)

Carlo approach described in Huber et al. (2013) to explore systematics introduced by our Bayesian pipeline. A comparison between our reference parameters and those derived with a different approach are shown in Figure 13. For stars with known seismic classification, differences are usually only a few percent, while they can grow considerably larger for stars without seismic classification.

For the final and global uncertainties in $\log g$ (and densities), radii, distances, and masses, we add quadratically to the

formal uncertainties from our BaSTI reference models half the difference between those results and the ones obtained with the GARSTEC grid and the Monte Carlo approach. Their median values are 82 K in $T_{\rm eff}$, 0.17 dex in [Fe/H], 0.006 dex in $\log g$, 1.5% in stellar density, 2.4% in radius, 3.3% in distance, and 6.0% in mass. As expected, the uncertainty in asteroseismic quantities is also smaller for stars with known evolutionary phase classification compared to stars for which this information in unknown (Figure 14). In all instances, it should be kept in

18
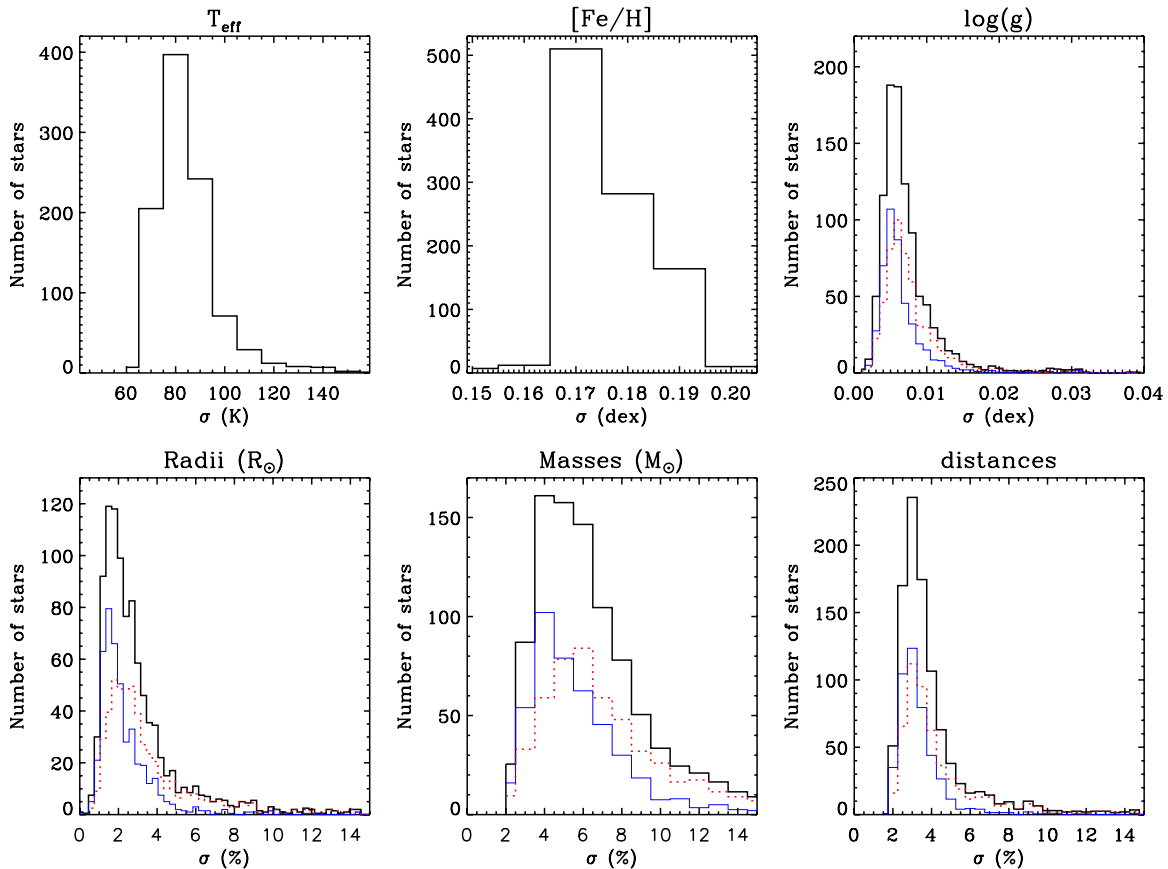
**Figure 14.** Final error distributions of the main stellar parameters derived. For the asteroseismic quantities, the overall distribution is also split into stars with (blue) and without (red) evolutionary phase classification (Section 3.4).

(A color version of this figure is available in the online journal.)

mind that while we have carefully accounted for various sources of uncertainties, the accuracy of the seismic parameters is currently limited by empirical tests of the scaling relations, which are assumed to be exact here.

### 3.8. Adopted Parameters

As already described, stellar parameters have been derived self-consistently for nine different combinations of photometric systems and reddening maps. We also verified in the previous section that the use of three different photometric systems in the IRFM did not introduce any major difference in the results and hence merged those, thus curbing our combinations to the three reddening maps. For our field, the symmetric and spiral model of Amôres & Lépine (2005) yield virtually identical results (Section 3.3), effectively meaning that we are dealing with two different sets of results.

Figure 15 compares the model (**v** in Equation (5)) and empirical effective temperatures (from the IRFM) derived with the two reddening maps. Note that the effective temperature is only one of many parameters entering our Bayesian scheme, and in fact, the model effective temperature barely changes when adopting a different reddening map (see the top left panel in Figure 12, where the mean and median differences are only 12 and 2 K, respectively). While differences might exist between the empirical and the model $T_{\rm eff}$ scale, the $\Delta T_{\rm eff}$ trend with respect to Galactic latitude in the Drimmel et al. (2003) case (Figure 15, right panel) recalls that of Figure 9 (lower right panel), thus dictating our preference for Amôres & Lépine

(2005). Note, however, that our reddening errors account for the difference between the two maps (Section 3.7).

To summarize, our photometric stellar parameters are derived adopting the Amôres & Lépine (2005) reddening map (rescaled to match the reddening of NGC 6819) with seismic parameters obtained using the BaSTI noncanonical isochrones with no mass loss and the global errors derived in Section 3.7 and shown in Figure 14. The catalog is available in the online journal, and Table 1 provides information about each tabular column. Depending on the purpose for which we use our parameters, we can also restrict our analysis to include only stars with more certain seismic classification.

### 3.9. External Validation of Derived Parameters

Throughout this paper we have used the open cluster NGC 6819 as a benchmark point. Here we used it to further check the consistency of the main parameters derived from the seismic analysis. Figure 16 shows the metallicity distribution of the seismic giants in the cluster: just as expected from the discussion of Section 3.2, the solar metallicity of this cluster is reproduced. More interesting is the second panel, which shows the distance distribution for the same stars. Their distance sharply peaks at a value of $2.38 \pm 0.08$ kpc, in excellent agreement with similar estimates obtained from isochrone fitting (e.g., Yang et al. 2013; Sandquist et al. 2013).

Figure 17 shows all seismic targets analyzed in this work in the empirical (IRFM) $T_{\rm eff}$–seismic $\log g$ plane: the very clear
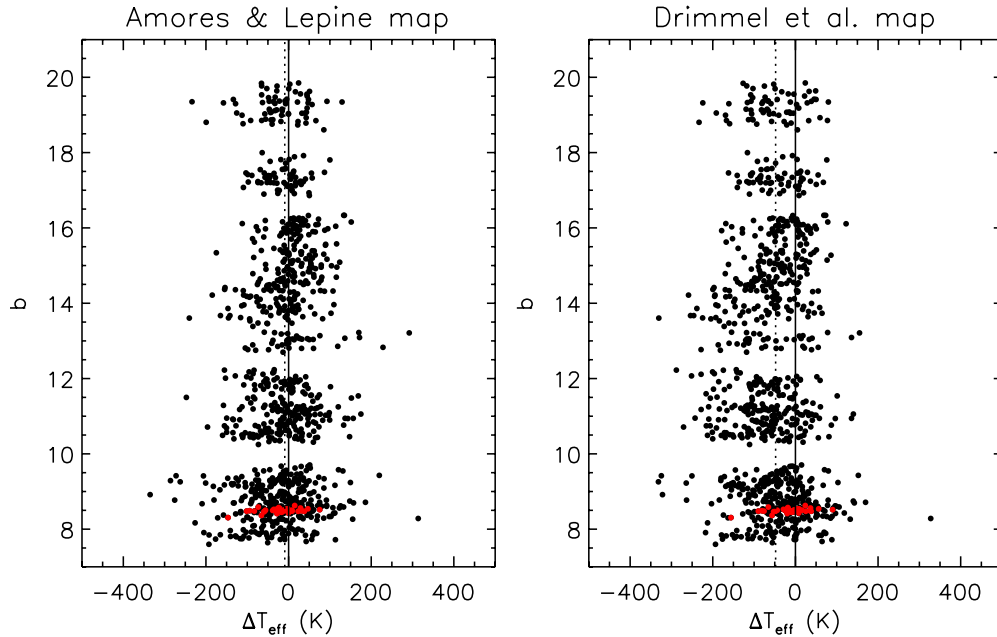
**Figure 15.** Difference between $T_{eff}$ obtained from the IRFM and from theoretical modeling for each star (IRFM minus models) as a function of Galactic latitude $b$ for two different reddening maps, as indicated. The dotted line is the median difference. At low $b$, stars belonging to NGC 6819 and used to calibrate both reddening maps are highlighted (see Section 3.3).

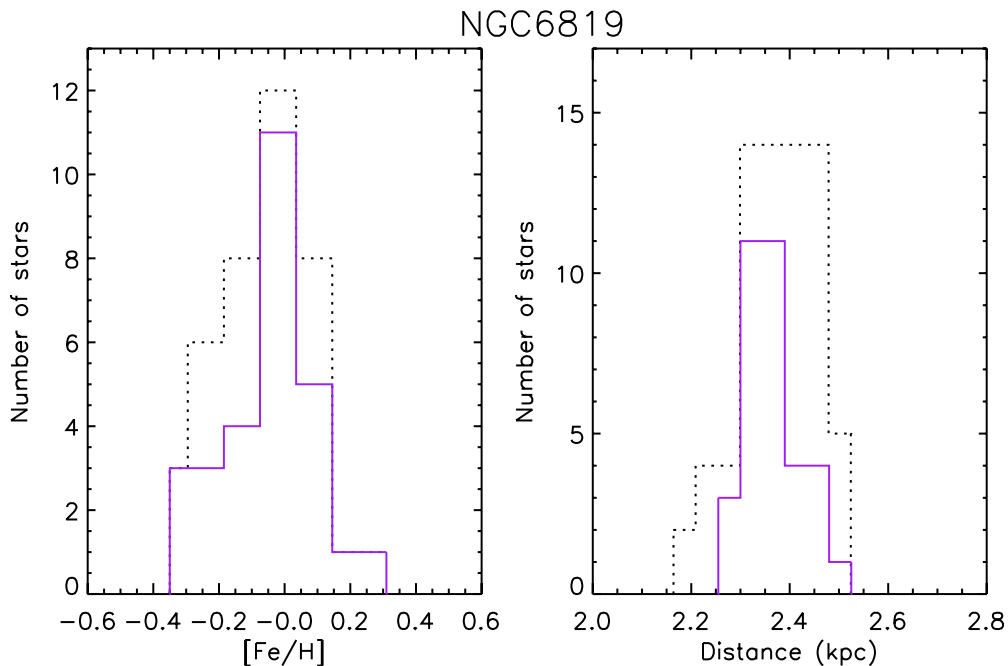(A color version of this figure is available in the online journal.)



**Figure 16.** Parameters determined for giants in the open cluster NGC 6819, selected according to the seismic classification of Stello et al. (2011). Left: metallicities for all stars (dotted line) or retaining only stars with a good photometric quality flag (continuous line; Section 2.3). Right: distances for the same stars. Now, the dotted line refers to all stars, while the continuous line is for stars having a certain seismic classification (Section 3.4).

(A color version of this figure is available in the online journal.)

presence of primary and secondary clump stars appears. The latter population was discovered by Girardi et al. (1998) using *Hipparcos* parallaxes, and its detection here clearly illustrates the precision we have achieved. Such a population is composed of stars with $M \gtrsim 1.8 M_\odot$ that ignite helium in nondegenerate conditions, and it is relatively short-lived, peaking at ∼1 Gyr (e.g., Girardi 1999, where the exact mass and age depend on the adopted models).

## 4. COMPARISON WITH OTHER WORKS

### 4.1. KIC

Currently, the largest database of stellar parameters for stars in the *Kepler* field is provided by the KIC (Brown et al. 2011), which was originally conceived as a tool to optimize the target selection (Batalha et al. 2010) and thus to provide only approximate estimates of stellar parameters. A number of

**Table 1**
SAGA Asteroseismic Catalog Format

| Column | Format | Description |
|---|---|---|
| 1 | A7 | KIC ID |
| 2 | A1 | Flag on KIC ID |
| 3 | F6.1 | Frequency of maximum oscillations power $\nu_{max}$ ($\mu$Hz) |
| 4 | F5.1 | Uncertainty in $\nu_{max}$ ($\mu$Hz) |
| 5 | F6.2 | Large frequency separation $\Delta\nu$ ($\mu$Hz) |
| 6 | F4.2 | Uncertainty in $\Delta\nu$ ($\mu$Hz) |
| 7 | F5.2 | Strömgren [Fe/H] (dex) |
| 8 | F4.2 | Uncertainty in Strömgren [Fe/H] |
| 9 | I4 | $T_{eff}$ from the IRFM (K) |
| 10 | I3 | Uncertainty in $T_{eff}$ |
| 11 | F5.2 | Stellar radius ($R_\odot$) |
| 12 | F5.2 | Upper uncertainty in stellar radius |
| 13 | F5.2 | Lower uncertainty in stellar radius |
| 14 | F4.2 | Stellar mass ($M_\odot$) |
| 15 | F4.2 | Upper uncertainty in stellar mass |
| 16 | F4.2 | Lower uncertainty in stellar mass |
| 17 | F5.3 | Surface gravity (dex) |
| 18 | F5.3 | Upper uncertainty in surface gravity |
| 19 | F5.3 | Lower uncertainty in surface gravity |
| 20 | F9.7 | Stellar density ($\rho_\odot$) |
| 21 | F9.7 | Upper uncertainty in stellar density |
| 22 | F9.7 | Lower uncertainty in stellar density |
| 23 | I4 | Distance from the Sun (pc) |
| 24 | I4 | Upper uncertainty in distance |
| 25 | I4 | Lower uncertainty in distance |
| 26 | A5 | Asteroseismic classification |
| 27 | I1 | Metallicity flag |
| 28 | I1 | Strömgren photometry flag |
| 29 | F5.3 | Strömgren $(b-y)$ index |
| 30 | F5.3 | Strömgren $m_1$ index |
| 31 | F5.3 | Strömgren $c_1$ index |

(This table is available in its entirety in a machine-readable form in the online journal. A portion is shown here for guidance regarding its form and content.)

investigations have highlighted inaccuracies in its parameters (e.g., Molenda-Żakowicz et al. 2011; Pinsonneault et al. 2012; Thygesen et al. 2012).

In Figure 18, we compare the SAGA $T_{eff}$ and [Fe/H] against the KIC. The effective temperatures of giants are in overall reasonable agreement (KIC being some 20 K hotter but with a large 80 K scatter), also considering uncertainties related to reddening. However, a clear offset appears when moving to main-sequence stars, spurring systematic differences by more than 200 K (SAGA being hotter). These trends are in agreement with similar findings for dwarfs by Pinsonneault et al. (2012) and for giants by Thygesen et al. (2012).

Concerning [Fe/H], the KIC performs less well. For giants $\Delta$[Fe/H] $= -0.13$ dex (SAGA minus KIC) and $\sigma = 0.35$ dex, which improves only moderately if restricting to stars with the most reliable Strömgren metallicities. Part of the scatter might arise from the fact that metallicities in the KIC are more representative of the overall metal content [M/H], while we calibrated our photometry using direct [Fe/H] measurements. Field stars in the Galactic disk are known to generally increase their [$\alpha$/Fe] content going toward lower metallicities (e.g., Tinsley 1979; McWilliam 1997; Matteucci 2001; Pagel 2009). If we assign [$\alpha$/Fe] to our stars according to the analytic model of Pagel & Tautvaisiene (1995) and compute their [M/H], the offset and the scatter reduce to $-0.07$ and 0.31 dex, respectively, with a particular improvement for stars with metallicities below $-1$ dex. A similar trend toward low metallicities in the KIC can also be seen in the comparison of Dong et al. (2013).
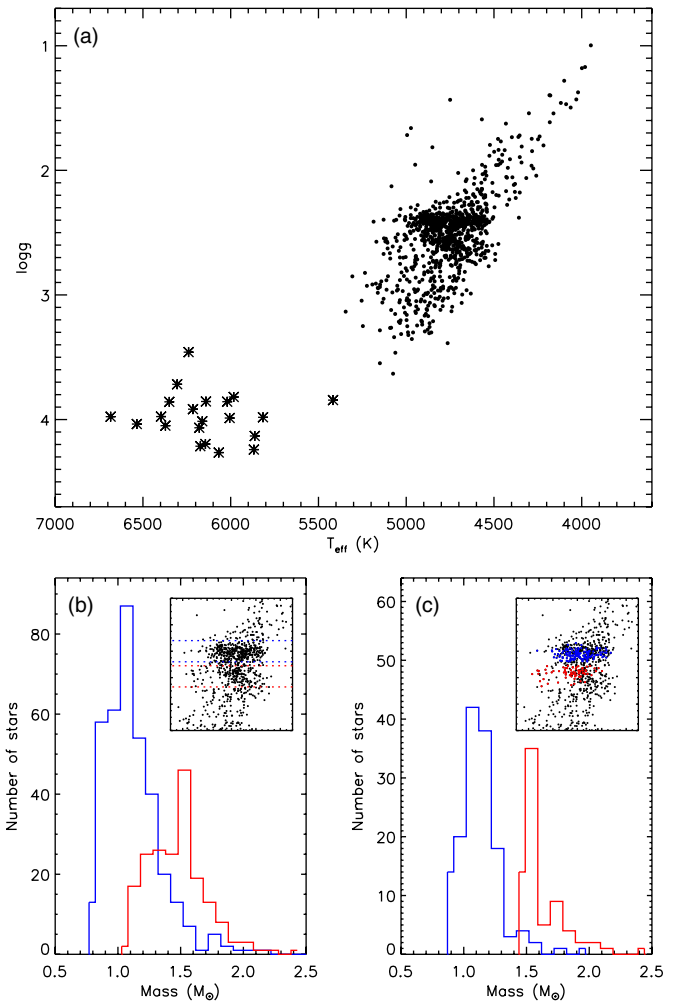


**Figure 17.** (a) $T_{eff}$ and $\log g$ for our sample of stars. Asterisks and circles identify stars for which we used the dwarf and giant metallicity calibrations, respectively (Section 3.2). (b) First (blue) and secondary (red) clump dissection based only on $\log g$ selection (range indicated by dotted lines in the upper inset) and the corresponding histogram for their mass distribution. (c) The same as in panel (b), but retaining only stars with a certain clump classification.
(A color version of this figure is available in the online journal.)

It is also interesting to compare our results with the reddening and surface gravities reported in the KIC. Confidence in the SAGA values of $E(B-V)$ comes from the fact that the good agreement of our photometric $T_{eff}$ with respect to spectroscopy (next section) disappears if the reddening of the KIC is adopted. Our calibrated reddening map indicates that the color excess reported in the KIC is increasingly overestimated for increasing values of $E(B-V)$. The correlation shown in Figure 19(a) also appears when the same quantity on the $y$-axis is plotted as a function of apparent magnitudes or distances (which in turn are highly correlated), thus indicating that fainter and farther away objects in the KIC are more likely to have inaccurate values of reddening. This suggests that the scale height and/or the attenuation adopted in the KIC dust model are the primary causes for this disagreement. Another spatial dependence appears when plotting the percent difference as a function of Galactic latitude $b$ (Figure 19(b)). At higher $b$ reddening decreases, but percentagewise the KIC overestimation is larger. A linear fit of the trend in Figure 19(a) accounts for most of the difference between the KIC and SAGA, but it does not remove the trend of the fractional error as a function of $b$. This is accounted for by fitting the
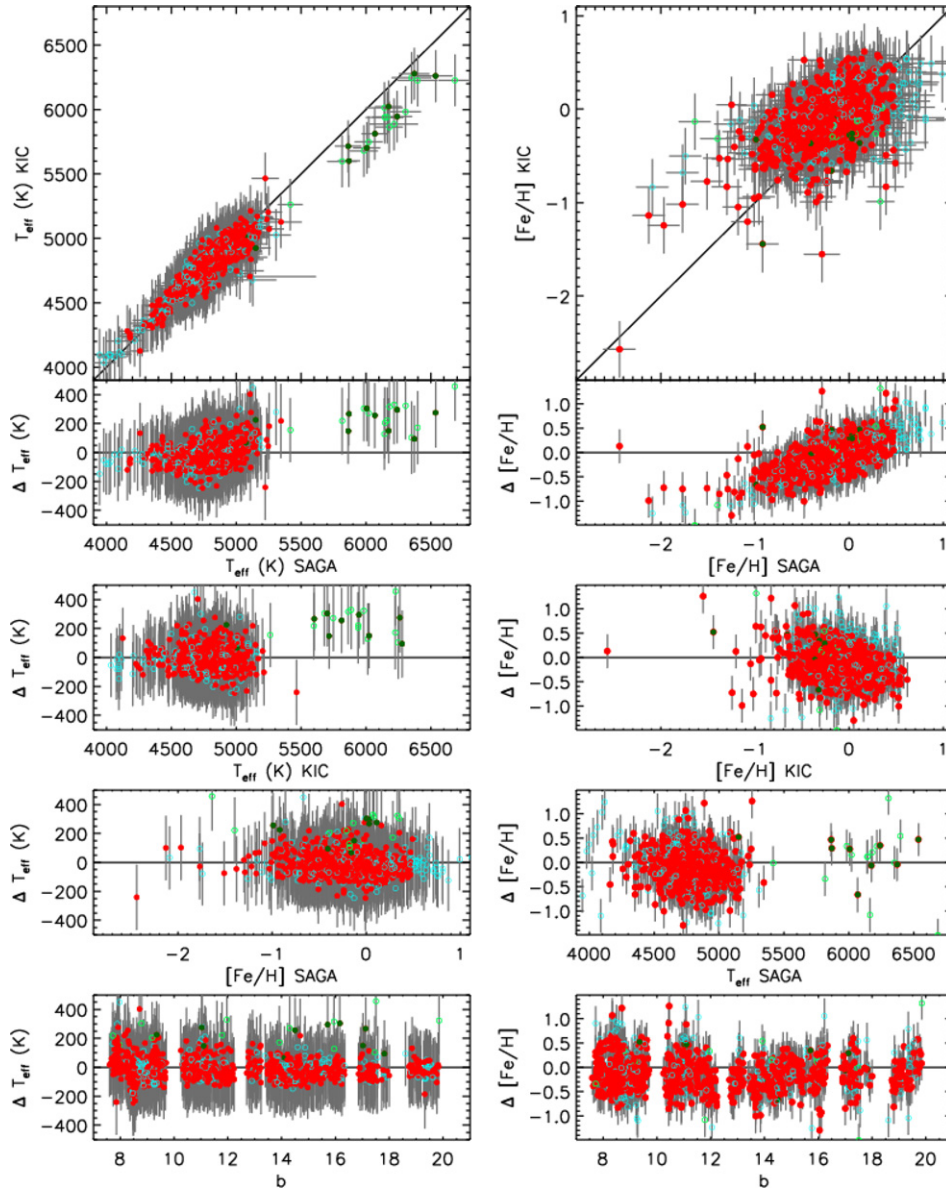
**Figure 18.** Comparison between $T_{\rm eff}$ (first column) and [Fe/H] (second column) determined for stars in the SAGA and KIC ($\Delta$ = SAGA minus KIC). Filled red and open cyan (filled dark green and open bright green) circles identify giants (dwarfs) with more certain and more uncertain Strömgren labels, respectively (see Section 3.2).
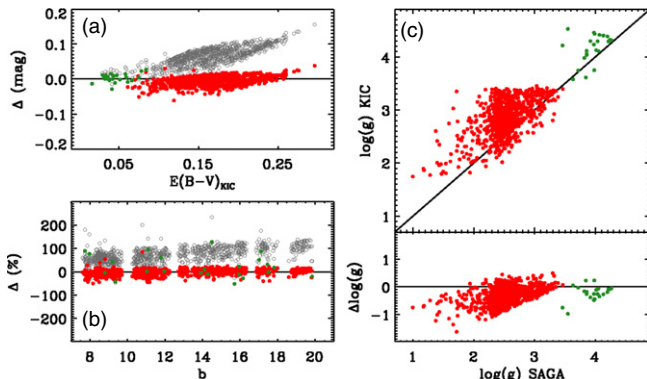(A color version of this figure is available in the online journal.)



**Figure 19.** (a) Comparison between the color excesses $E(B-V)$ in the KIC and SAGA (gray circles, KIC minus SAGA). Colored circles (green for dwarfs, red for giants) highlight the same comparison after correcting the KIC reddening according to Equation (9). (b) The same as in panel (a), but showing the percent difference (KIC/SAGA) as a function of Galactic latitude. (c) Comparison between $\log g$ in the KIC and asteroseismic values in SAGA.
(A color version of this figure is available in the online journal.)

ratio between the color excess in SAGA and the values obtained from the linear fit above. The corrected reddening we derive for the color excess in the KIC is thus

$$E(B-V) = [0.55\,E(B-V)_{\rm KIC} + 0.008](1.2 - 0.02\,b), \quad (9)$$

where the first term is dominant, while the second accounts for the spatial dependency of the fractional difference. Since all reddening values in the KIC are derived using the same dust model, the correction proposed here likely applies for most of the stars in the *Kepler* field. It should be kept in mind that Equation (9) is tailored to the stripe analyzed in this work.

Figure 19(c) compares the surface gravities we derived from asteroseismology with the values reported in the KIC. The sharp cut at $\log g \sim 3.4$ reflects the KIC-based preselection of giants for measuring oscillations (Ciardi et al. 2011; Hekker et al. 2011b). We have already discussed in Section 3.7 the precision of asteroseismic gravities; $\log g$ values in the KIC were derived with the purpose of broadly distinguishing between dwarfs and
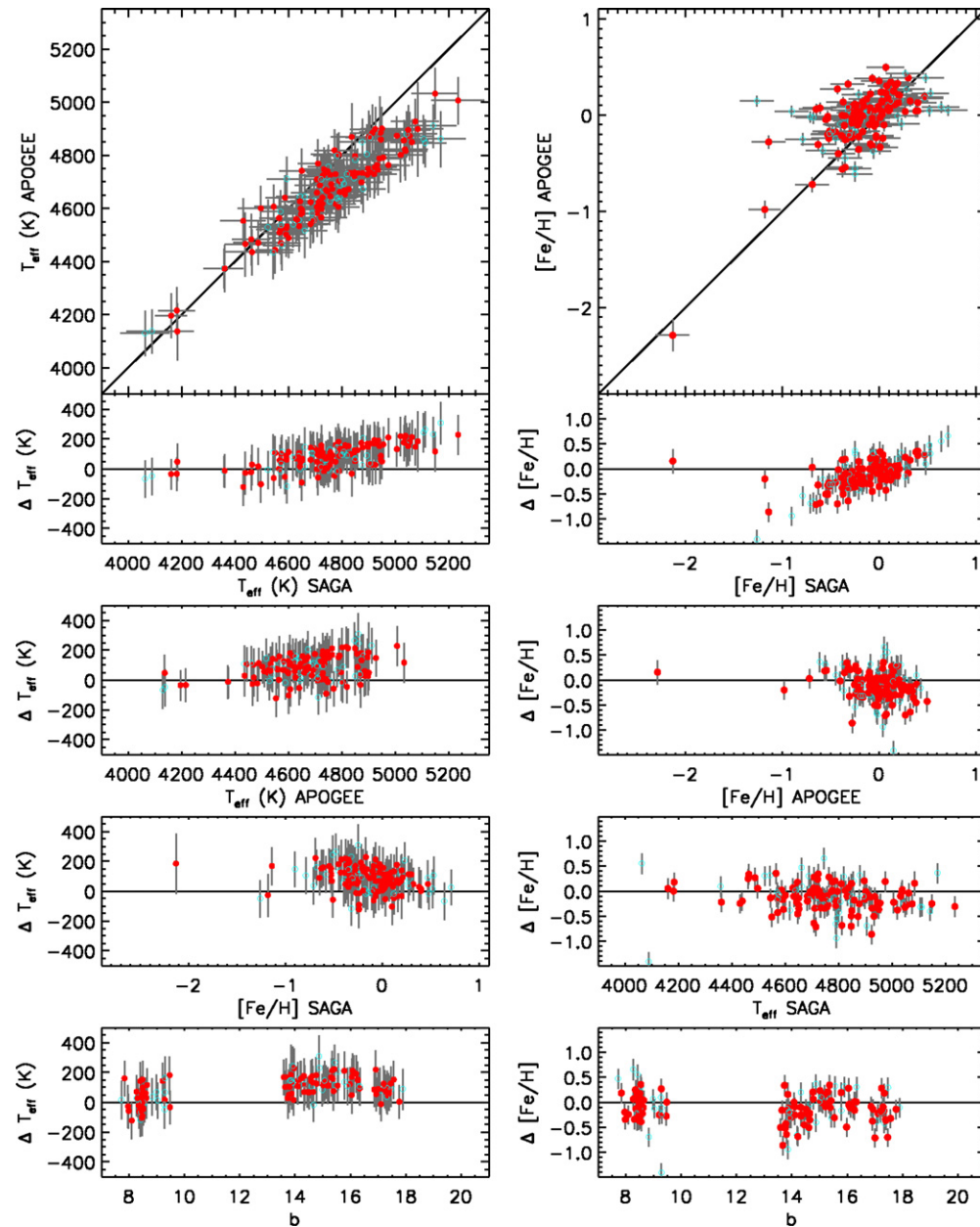
**Figure 20.** Same as Figure 18, but comparing giants in SAGA with APOGEE ($\Delta$ = SAGA minus APOGEE).
(A color version of this figure is available in the online journal.)

giant, and we confirm here the overall success in doing this (but see Huber et al. 2014 for a more detailed discussion).

### 4.2. APOGEE

The APOGEE uses high-resolution $H$-band spectra to observe some $10^5$ giants across the Galaxy (Ahn et al. 2014). As part of this project, a number of targets in the *Kepler* field have been observed and are now publicly available via DR10. In Figure 20, we compare our SAGA parameters with the spectroscopic ones from APOGEE. Details on the derivation of those can be found in Mészáros et al. (2013). Briefly, two sets of parameters are provided: raw and corrected $T_{\rm eff}$ and [Fe/H]. Corrections for the latter are determined from fitting polynomials to reproduce a number of benchmark stars and clusters and amount to 0.2 dex in metallicity and 100 K in $T_{\rm eff}$ for the stars used here. The

comparison carried out here is with respect to the corrected APOGEE parameters.

The agreement in $T_{\rm eff}$ is good overall, with $\Delta T_{\rm eff} = 90 \pm 105$ K, with SAGA being hotter. It is particularly good below $\simeq 4600$ K ($\Delta T_{\rm eff} = 0 \pm 34$ K), although APOGEE tends to increasingly underestimate $T_{\rm eff}$ descending the RGB toward hotter stars. Concerning metallicities, the comparison looks tighter because of the much higher quality of the APOGEE parameters with respect to the KIC. The same trend already highlighted in Figure 18 appears, although it is not as dramatic when we restrict the sample to stars with the best Strömgren photometry, $\Delta$[Fe/H] $= -0.11 \pm 0.26$ dex (only slightly larger than expected considering uncertainties in the SAGA and APOGEE values). While the raw APOGEE metallicities are more representative of the global [M/H], their corrected ones are forced to reproduce [Fe/H] of a number of benchmark

clusters (see the discussion in Mészáros et al. 2013). A few of these clusters are also used for our metallicity calibration: using for them the same [Fe/H] adopted by APOGEE changes our metallicities at the level of 0.1 dex toward the metal-poor regime.

## 5. CONCLUSIONS

In this paper, we have presented Strömgren photometry of a stripe in the *Kepler* field. While the ultimate purpose is to use these observations to provide homogeneous and reliable stellar parameters for both candidate planet host and seismic stars, the geometry chosen for our observations already enables Galactic studies using stars with detected oscillations.

The strength of our approach is in the coupling of classical and asteroseismic parameters: effective temperatures (from the IRFM, metallicities (from Strömgren indices), masses, and radii (from seismology) are derived iteratively and self-consistently, thus giving access to other quantities such as reddening and distances and providing a complete picture of the seismic population in our observed Galactic fields.

The open cluster NGC 6819 is located at the base of the observed stripe and offers an important benchmark to verify the soundness of our results. In particular, it allows us to anchor the metallicity scale of giants on the same zero point used for investigating properties in the solar neighborhood via dwarfs and subgiants from the GCS (Casagrande et al. 2011). This is crucial if, for example, we wish to use nearby stars and/or giants (up to $\simeq 6$ kpc across the Galactic disk in this work) for the purpose of understanding the formation and evolution of stellar populations in the Milky Way.

The sample presented here covers latitudes between $8°$ and $20°$ above the Galactic plane. The stellar parameters derived here are already well suited for a number of investigations; in particular, the seismic classification allows us to distinguish between stars ascending the RGB burning hydrogen in a shell and those that also have ignited helium burning in their core. Concerning the latter, the precision achieved allows us to discern between primary and secondary clumps and hence whether the core ignites degenerately or not. With this information and the parameters so far derived, we are thus in the position of using these stars to compute reliable stellar ages and investigate, for example, the age–metallicity relation and the age and metallicity gradients across this part of the Galactic disk. Furthermore, calibrating photometric metallicities and age-dating techniques on the present sample, a deep all-sky Strömgren survey promises a leading role for Galactic studies.

## REFERENCES

Aden, D. 2011, PhD thesis, Department of Astronomy and Theoretical Physics, Lund Univ.
Adén, D., Feltzing, S., Koch, A., et al. 2009, A&A, 506, 1147
Adibekyan, V. Z., Figueira, P., Santos, N. C., et al. 2013, A&A, 554, A44
Ahn, C. P., Alexandroff, R., Allende Prieto, C., et al. 2014, ApJS, 211, 17
Alonso, A., Arribas, S., & Martinez-Roger, C. 1996, A&AS, 117, 227
Alonso, A., Arribas, S., & Martínez-Roger, C. 1999, A&AS, 140, 261
Amôres, E. B., & Lépine, J. R. D. 2005, AJ, 130, 659
Árnadóttir, A. S., Feltzing, S., & Lundström, I. 2010, A&A, 521, A40
Baglin, A., & Fridlund, M. 2006, in The CoRoT Mission Pre-Launch Status—Stellar Seismology and Planet Finding, ed. M. Fridlund, A. Baglin, J. Lochard, & L. Conroy (ESA SP-1306; Noordwijk, The Netherlands), 11
Batalha, N. M., Borucki, W. J., Koch, D. G., et al. 2010, ApJL, 713, L109
Batalha, N. M., Rowe, J. F., Bryson, S. T., et al. 2013, ApJS, 204, 24
Bedding, T. R. 2011, in Asteroseismology, Canary Islands Winter School of Astrophysics, Vol. 22, ed. P. L. Palle (Cambridge: Cambridge Univ. Press)
Bedding, T. R., Mosser, B., Huber, D., et al. 2011, Natur, 471, 608
Bensby, T., Feltzing, S., & Oey, M. S. 2014, A&A, 562, 71
Bessell, M. S. 2005, ARA&A, 43, 293
Bird, J. C., Kazantzidis, S., Weinberg, D. H., et al. 2013, ApJ, 773, 43
Bragaglia, A., Carretta, E., Gratton, R. G., et al. 2001, AJ, 121, 327
Brown, T. M., Gilliland, R. L., Noyes, R. W., & Ramsey, L. W. 1991, ApJ, 368, 599
Brown, T. M., Latham, D. W., Everett, M. E., & Esquerdo, G. A. 2011, AJ, 142, 112
Calamida, A., Bono, G., Stetson, P. B., et al. 2007, ApJ, 670, 400
Carigi, L., & Peimbert, M. 2008, RMxAA, 44, 341
Carretta, E., Bragaglia, A., Gratton, R., D'Orazi, V., & Lucatello, S. 2011, A&A, 535, A121
Carretta, E., Bragaglia, A., Gratton, R. G., et al. 2009, A&A, 505, 117
Casagrande, L., Flynn, C., Portinari, L., Girardi, L., & Jimenez, R. 2007, MNRAS, 382, 1516
Casagrande, L., Portinari, L., & Flynn, C. 2006, MNRAS, 373, 13
Casagrande, L., Portinari, L., Glass, I. S., et al. 2014, MNRAS, 439, 2060
Casagrande, L., Ramírez, I., Meléndez, J., & Asplund, M. 2012, ApJ, 761, 16
Casagrande, L., Ramírez, I., Meléndez, J., Bessell, M., & Asplund, M. 2010, A&A, 512, A54
Casagrande, L., Schönrich, R., Asplund, M., et al. 2011, A&A, 530, A138
Casagrande, L., & VandenBerg, D. 2014, MNRAS, submitted
Cescutti, G., Matteucci, F., François, P., & Chiappini, C. 2007, A&A, 462, 943
Chaplin, W. J., Basu, S., Huber, D., et al. 2014, ApJS, 210, 1
Chaplin, W. J., Kjeldsen, H., Christensen-Dalsgaard, J., et al. 2011, Sci, 332, 213
Chaplin, W. J., & Miglio, A. 2013, ARA&A, 51, 353
Ciardi, D. R., von Braun, K., Bryden, G., et al. 2011, AJ, 141, 108
Cohen, J. G. 2011, ApJL, 740, L38
Corsaro, E., Fröhlich, H.-E., Bonanno, A., et al. 2013, MNRAS, 430, 2313
Crawford, D. L. 1975, AJ, 80, 955
Creevey, O. L., Thévenin, F., Basu, S., et al. 2013, MNRAS, 431, 2419
De Ridder, J., Barban, C., Baudin, F., et al. 2009, Natur, 459, 398
Dong, S., Zheng, Z., & Zhu, Z. 2013, arXiv:1311.1203
Drew, J. E., Greimel, R., Irwin, M. J., et al. 2005, MNRAS, 362, 753
Drimmel, R., Cabrera-Lavers, A., & López-Corredoira, M. 2003, A&A, 409, 205
Eggen, O. J., Lynden-Bell, D., & Sandage, A. R. 1962, ApJ, 136, 748
Faria, D., Feltzing, S., Lundström, I., et al. 2007, A&A, 465, 357
Farmer, R., Kolb, U., & Norton, A. J. 2013, MNRAS, 433, 1133
Feltzing, S., & Bensby, T. 2008, PhST, 133, 014031
Frankowski, A., Famaey, B., van Eck, S., et al. 2009, A&A, 498, 479
Freeman, K., & HERMES/GALAH Team 2014, BAAS, 223, 142
Gai, N., Basu, S., Chaplin, W. J., & Elsworth, Y. 2011, ApJ, 730, 63
García, R. A., Hekker, S., Stello, D., et al. 2011, MNRAS, 414, L6
Gilliland, R. L., Brown, T. M., Christensen-Dalsgaard, J., et al. 2010, PASP, 122, 131
Gilmore, G., Randich, S., Asplund, M., et al. 2012, Msngr, 147, 25
Girardi, L. 1999, MNRAS, 308, 818
Girardi, L., Groenewegen, M. A. T., Weiss, A., & Salaris, M. 1998, MNRAS, 301, 149
Gliese, W. 1957, MiARI, 8, 1

Grebel, E. K., & Richtler, T. 1992, A&A, 253, 359
Greiss, S., Steeghs, D., Gänsicke, B. T., et al. 2012, AJ, 144, 24
Groot, P. J., Verbeek, K., Greimel, R., et al. 2009, MNRAS, 399, 323
Grundahl, F., Stetson, P. B., & Andersen, M. I. 2002, A&A, 395, 481
Grundahl, F., Vandenberg, D. A., & Andersen, M. I. 1998, ApJL, 500, L179
Grundahl, F., VandenBerg, D. A., Bell, R. A., Andersen, M. I., & Stetson, P. B. 2000, AJ, 120, 1884
Gustafsson, B., Edvardsson, B., Eriksson, K., et al. 2008, A&A, 486, 951
Harris, W. E. 1996, AJ, 112, 1487
Harris, W. E., Fitzgerald, M. P., & Reed, B. C. 1981, PASP, 93, 507
Haywood, M. 2002, MNRAS, 337, 151
Hekker, S., Elsworth, Y., De Ridder, J., et al. 2011a, A&A, 525, A131
Hekker, S., Gilliland, R. L., Elsworth, Y., et al. 2011b, MNRAS, 414, 2594
Hilker, M. 2000, A&A, 355, 994
Hole, K. T., Geller, A. M., Mathieu, R. D., et al. 2009, AJ, 138, 159
Huber, D., Bedding, T. R., Stello, D., et al. 2011, ApJ, 743, 143
Huber, D., Chaplin, W. J., Christensen-Dalsgaard, J., et al. 2013, ApJ, 767, 127
Huber, D., Ireland, M. J., Bedding, T. R., et al. 2012, ApJ, 760, 32
Huber, D., Silva Aguirre, V., Matthews, J. M., et al. 2014, ApJS, 211, 2
Huber, D., Stello, D., Bedding, T. R., et al. 2009, CoAst, 160, 74
Irwin, M., & Lewis, J. 2001, NewAR, 45, 105
Jeffries, M. W., Jr., Sandquist, E. L., Mathieu, R. D., et al. 2013, AJ, 146, 58
Jenkins, J. M., Caldwell, D. A., Chandrasekaran, H., et al. 2010, ApJL, 713, L120
Jørgensen, B. R., & Lindegren, L. 2005, A&A, 436, 127
Kjeldsen, H., & Bedding, T. R. 1995, A&A, 293, 87
Kobayashi, C., & Nakasato, N. 2011, ApJ, 729, 16
Korn, A. J., Grundahl, F., Richard, O., et al. 2007, ApJ, 671, 402
Lebreton, Y., & Montalbán, J. 2009, in IAU Symp. 258, The Ages of Stars, ed. E. E. Mamajek, D. R. Soderblom, & R. F. G. Wyse (Cambridge: Cambridge Univ. Press), 419
Lind, K., Charbonnel, C., Decressin, T., et al. 2011, A&A, 527, A148
Lindegren, L., & Perryman, M. A. C. 1996, A&AS, 116, 579
Liu, C., Bailer-Jones, C. A. L., Sordo, R., et al. 2012, MNRAS, 426, 2463
Maeder, A. 1992, A&A, 264, 105
Massey, P., & Davis, L. E. 1992, in ASP Conf. Ser. 189, A User's Guide to Stellar CCD Photometry with IRAF, ed. E. R. Craine, D. L. Crawford, & R. A. Tucker (San Francisco, CA: ASP), 35
Matteucci, F. (ed.) 2001, The Chemical Evolution of the Galaxy (Astrophysics and Space Science Library, Vol. 253; Dordrecht: Kluwer)
McWilliam, A. 1997, ARA&A, 35, 503
Meléndez, J., Schuster, W. J., Silva, J. S., et al. 2010, A&A, 522, A98
Mészáros, S., Holtzman, J., García Pérez, A. E., et al. 2013, AJ, 146, 133
Miglio, A., Brogaard, K., Stello, D., et al. 2012, MNRAS, 419, 2077
Miglio, A., Chiappini, C., Morel, T., et al. 2013a, MNRAS, 429, 423
Miglio, A., Montalbn, J., Baudin, F., et al. 2009, A&A, 503, L21
Miglio, A., Chiappini, C., Morel, T., et al. 2013b, EPJWC, 43, 3004
Milone, A. P., Marino, A. F., Piotto, G., et al. 2012a, ApJ, 745, 27
Milone, A. P., Piotto, G., Bedin, L. R., et al. 2012b, A&A, 540, A16
Minchev, I., Chiappini, C., & Martig, M. 2013, A&A, 558, 9
Minniti, D., Lucas, P. W., Emerson, J. P., et al. 2010, NewA, 15, 433
Molenda-Żakowicz, J., Latham, D. W., Catanzaro, G., Frasca, A., & Quinn, S. N. 2011, MNRAS, 412, 1210
Montalbán, J., Miglio, A., Noels, A., et al. 2013, ApJ, 766, 118
Morel, T., & Miglio, A. 2012, MNRAS, 419, L34
Mosser, B., Goupil, M. J., Belkacem, K., et al. 2012, A&A, 540, 143
Nataf, D. M., Gould, A., & Pinsonneault, M. H. 2012, AcA, 62, 33
Nordström, B., Mayor, M., Andersen, J., et al. 2004, A&A, 418, 989
Olsen, E. H. 1983, A&AS, 54, 55
Olsen, E. H. 1984, A&AS, 57, 443

Olsen, E. H. 1994a, A&AS, 104, 429
Olsen, E. H. 1994b, A&AS, 106, 257
Önehag, A., Gustafsson, B., Eriksson, K., & Edvardsson, B. 2009, A&A, 498, 527
Pagel, B. E. J. 2009, Nucleosynthesis and Chemical Evolution of Galaxies (Cambridge: Cambridge Univ. Press)
Pagel, B. E. J., & Tautvaisiene, G. 1995, MNRAS, 276, 505
Perryman, M. A. C., de Boer, K. S., Gilmore, G., et al. 2001, A&A, 369, 339
Pietrinferni, A., Cassisi, S., Salaris, M., & Castelli, F. 2004, ApJ, 612, 168
Pilkington, K., Gibson, B. K., Brook, C. B., et al. 2012, MNRAS, 425, 969
Pinsonneault, M. H., An, D., Molenda-Żakowicz, J., et al. 2012, ApJS, 199, 30
Platais, I., Gosnell, N. M., Meibom, S., et al. 2013, AJ, 146, 43
Plavchan, P., Bilinski, C., & Currie, T. 2014, PASP, 126, 34
Pont, F., & Eyer, L. 2004, MNRAS, 351, 487
Reddy, B. E., Lambert, D. L., & Allende Prieto, C. 2006, MNRAS, 367, 1329
Reid, I. N., & Hawley, S. L. 2005, New Light on Dark Stars: Red Dwarfs, Low-mass Stars, Brown Dwarfs (Chichester, UK: Praxis)
Reimers, D. 1975, MSRSL, 8, 369
Roederer, I. U., & Sneden, C. 2011, AJ, 142, 22
Rosvick, J. M., & Vandenberg, D. A. 1998, AJ, 115, 1516
Sandquist, E. L., Mathieu, R. D., Brogaard, K., et al. 2013, ApJ, 762, 58
Savitzky, A., & Golay, M. J. E. 1964, AnaCh, 36, 1627
Schlegel, D. J., Finkbeiner, D. P., & Davis, M. 1998, ApJ, 500, 525
Schönrich, R., & Binney, J. 2009, MNRAS, 396, 203
Schuster, W. J., & Nissen, P. E. 1988, A&AS, 73, 225
Schuster, W. J., & Nissen, P. E. 1989, A&A, 221, 65
Serenelli, A. M., Bergemann, M., Ruchti, G., & Casagrande, L. 2013, MNRAS, 429, 3645
Silva Aguirre, V., Basu, S., Brando, I. M., et al. 2013, ApJ, 769, 141
Silva Aguirre, V., Casagrande, L., Basu, S., et al. 2012, ApJ, 757, 99
Silva Aguirre, V., Chaplin, W. J., Ballot, J., et al. 2011, ApJL, 740, L2
Skrutskie, M. F., Cutri, R. M., Stiening, R., et al. 2006, AJ, 131, 1163
Sneden, C., Kraft, R. P., Guhathakurta, P., Peterson, R. C., & Fulbright, J. P. 2004, AJ, 127, 2162
Soderblom, D. R. 2010, ARA&A, 48, 581
Steinmetz, M., Zwitter, T., Siebert, A., et al. 2006, AJ, 132, 1645
Stello, D., Chaplin, W. J., Basu, S., Elsworth, Y., & Bedding, T. R. 2009, MNRAS, 400, L80
Stello, D., Huber, D., Bedding, T. R., et al. 2013, ApJL, 765, L41
Stello, D., Meibom, S., Gilliland, R. L., et al. 2011, ApJ, 739, 13
Strömgren, B. 1963, QJRAS, 4, 8
Strömgren, B. 1966, ARA&A, 4, 433
Strömgren, B. 1987, in NATO ASIC Proc. 207, The Galaxy, ed. G. Gilmore & B. Carswell (Dordrecht: Reidel), 229
Thygesen, A. O., Frandsen, S., Bruntt, H., et al. 2012, A&A, 543, A160
Tinsley, B. M. 1979, ApJ, 229, 1046
Twarog, B. A., Vargas, L. C., & Anthony-Twarog, B. J. 2007, AJ, 134, 1777
Ulrich, R. K. 1986, ApJL, 306, L37
van den Bergh, S. 1962, AJ, 67, 486
Verner, G. A., Elsworth, Y., Chaplin, W. J., et al. 2011, MNRAS, 415, 3539
Wallerstein, G. 1962, ApJS, 6, 407
Wang, W., Zhao, G., & Chen, Y. 2014, in Proc. IAU Symp. 298, Setting the Scene for Gaia and LAMOST, ed. S. Feltzing, G. Zhao, N. A. Walton, & P. A. Whitelock (Cambridge: Cambridge Univ. Press)
Wang, Y., & Zhao, G. 2013, ApJ, 769, 4
Weiss, A., & Schlattl, H. 2008, Ap&SS, 316, 99
White, T. R., Huber, D., Maestro, V., et al. 2013, MNRAS, 433, 1262
Yang, S.-C., Sarajedini, A., Deliyannis, C. P., et al. 2013, ApJ, 762, 3
Yanny, B., Rockosi, C., Newberg, H. J., et al. 2009, AJ, 137, 4377
Yong, D., Grundahl, F., Johnson, J. A., & Asplund, M. 2008, ApJ, 684, 1159